2

Urban Radio Access Networks

Sana Salous, Thomas Werthmann, Ghassan Dahman, Jose Flordelis, Michael Peter, Sooyoung Hur, Jeongho. Jh. Park, Denis Rose and Andrés Navarro

The increase in demand for high-data rates on the move in the complex urban environment requires either the allocation of new spectrum such as available contiguous spectrum in the mm-wave band or the use of novel configurations such as the application of massive multiple-input multiple-output (MIMO) technology. To enable the design of efficient wireless networks, an understanding of the propagation phenomena in the diverse urban environments is fundamental. In this chapter, we present results of studies related to fourth generation (4G) and future 5G radio systems both outdoor and outdoor-to-indoor. Classifications include rural and highway, BS to pedestrian users, vehicular-to-vehicular, vehicular-to-infrastructure, container terminals, vegetation, and high-speed mobility such as trains. Results for path loss (PL) and shadow fading are presented from various studies of stochastic and deterministic channel models based in outdoor, indoor-to-outdoor, hotspots, vehicular, and train environments. Relay stations and the impact of antenna placement in vehicles, antenna terminal height, and the presence of pedestrians are discussed. Results of angular spread and *rms* delay spread of wideband channels are presented for the frequency bands below 6 GHz allocated for 4G networks, and preliminary results in the mm-wave band, envisaged for 5G networks, including prediction of the impact of rain. To facilitate the simulation of radio networks in urban environments the Hannover Scenario is proposed to give a common simulation environment.

2.1 Radio Propagation in Urban Scenarios

2.1.1 Radio Propagation Measurement and Stochastic Modelling

In this section, updated channel parameters for various urban environments are reported in Section 2.1.1.1. Section 2.1.1.2 reports measurement results

Cooperative Radio Communications for Green Smart Environments, 17–70.

in challenging conditions such as container terminals, rain, vegetation and trains. In Section 2.1.1.3, results on the effect of the user mobility, existence of pedestrians, and transmit/receive antenna height on the channel parameters are reported.

2.1.1.1 Channel characterisation in various urban scenarios

Relay

Extensive measurements were performed to study the statistics of shadow fading in relay links and the correlation of shadow fading between a BS-mobile station (MS) link and a RS-MS link or between two RS-MS links [CM12, CCC11]. In the work by Chu et al. [CCC11], shadow fading is modelled as a zero-mean log-normal distribution with 5–11 dB standard deviation (STD). For each RS location, the correlation of shadow fading with the same RS-MS link was calculated for three different RS antenna heights: (4.7, 8.8, and 12.7 m). The correlation of shadow fading of the same RS-MS link for the different RS antenna height was found to be 0.75–0.96, indicating high correlation. However, the correlation of the shadow fading between the BS-MS, and the RS-MS links (and also between two RS-MS links), varied from –0.04 to 0.57. The correlation values were found to be inversely proportional to the difference angle between the two considered links. For an angular difference less than 10°, high-correlation values from 0.4 to 0.6 were found. When the difference angle increased to about 60°–80°, the correlation coefficients rapidly decreased towards zero as seen in Figure 2.1. The correlation also decreases when the distance between transmitters (TXs) increases. Moreover, the highest coefficient of about 0.5 was observed between TX pairs having a small separation as illustrated in Figure 2.2.

The PL model was studied in the work by Conrat and Maaz [CF12, CM13, CM14], where the relay antenna height was found to have an impact on the model in non-line-of-sight (NLoS) propagation. In the paper by Conrat and Maaz [CM13], the line-of-sight (LOS) PL was found to consist of two distance zones called the near zone (20–30 m from the RS) and the far zone. For the near zone, the PL depends on the antenna gains of the RS and the MS but generally remains flat and thus the log-distance model is not applicable as seen in Figure 2.3. For the far zone, the free-space log-distance model with an additional term representing a shift of about ± 6 dB is suggested to be added in order to incorporate the effect of the RS position Equation (2.1).

$$\mathrm{PL_{dB}} = 20\log_{10}(d) + 39 + \mathrm{EF} + \mathrm{SF}, \tag{2.1}$$

where, SF is a Gaussian variable with a STD of 5.8 dB, and EF is uniformly distributed random variable ± 6 dB.

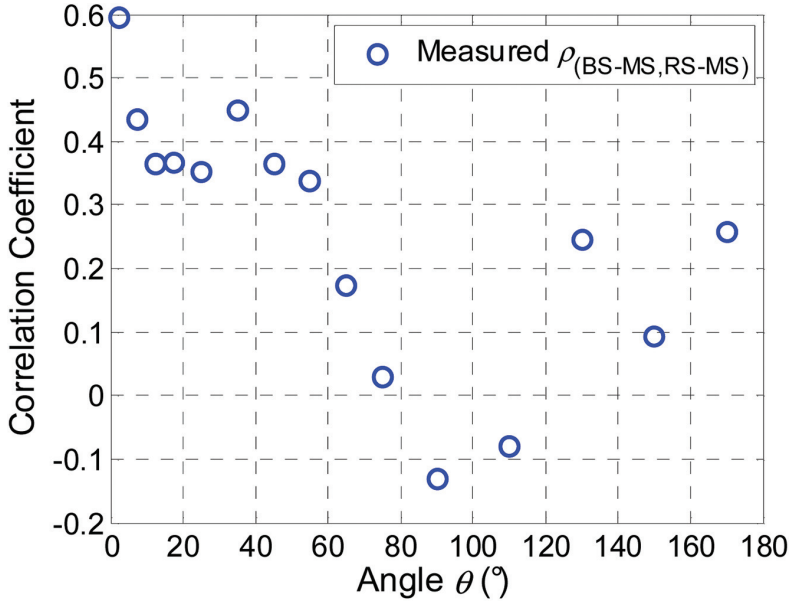

(a)

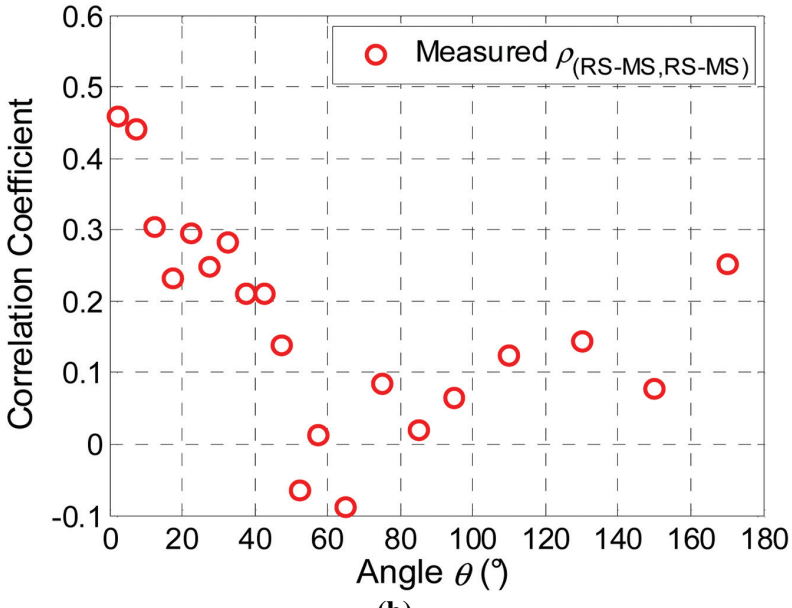

(b)

Figure 2.1 Measured shadow fading correlation versus difference angle: (a) $\rho_{(\text{BS-MS,RS-MS})}$, and (b) $\rho_{(\text{RS-MS,RS-MS})}$.

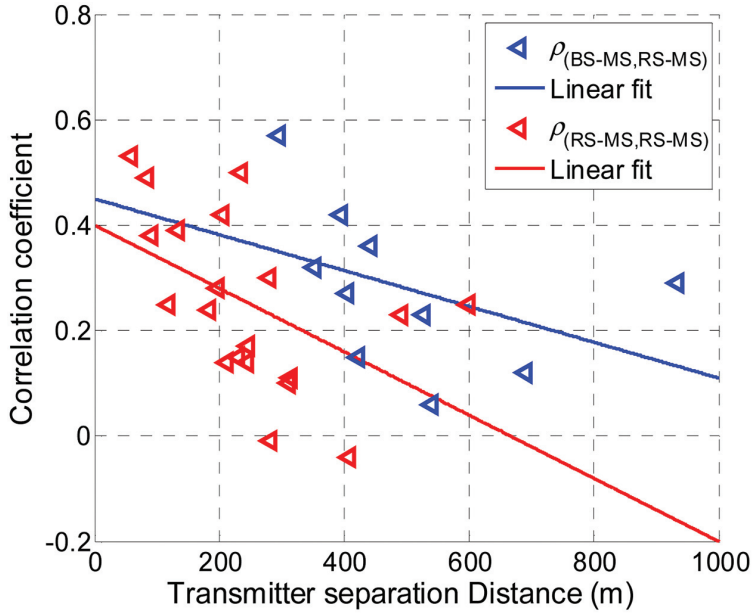

Figure 2.2 Dependence of shadow fading correlation on the TX separation distance.

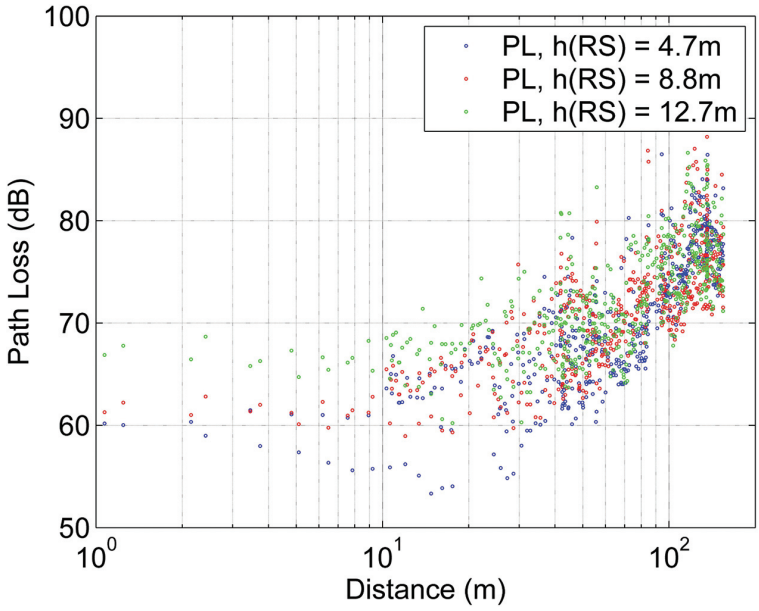

Figure 2.3 Flat zone example.

In the NLoS case, the PL is affected by the RS antenna height and the PL model can be presented as in Equation (2.2).

$$\mathrm{PL_{dB}} = 46\log_{10}(d) + 14.2 - 0.6\,h_{\mathrm{RS}} + \mathrm{SF}, \tag{2.2}$$

where, SF is a Gaussian variable with a STD of 9.6 dB, and h_{RS} is the RS antenna height.

In Conrat and Maaz [CF12], a simple refined PL model is introduced based on existing PL models with an antenna height correction factor. A measurement-based comparison was performed in the work by Conrat and Maaz [CM15] and it showed that the COST231 WI and wireless world initiative new radio (WINNER)+PL models overestimate the PL prediction. However, models proposed by 3rd generation partnership project (3GPP) and the ITU give the best performance.

In Yin et al. [YPKC12], the cross-correlation of small-scale fading (SSF) was evaluated for different locations of the base station (BS), relay station and mobile station in a three-node cooperative relay system. SSF was found to be more correlated when (i) the difference angle between the direct links from the BS to the MS and from the RS to the MS decreases; (ii) when the MS has similar distance to the BS and to the RS; and (iii) when the MS moves away from the region where the BS and RS are located.

Outdoor to/from indoor

The PL from outdoor-to-indoor at three different frequency bands 700, 450, and 150 MHz were compared in the work Bultitude et al. [BSCZ12]. It was found that the absolute and the excess outdoor-to-indoor propagation losses were highest in the 700-MHz band. Figure 2.4 shows the CCDF for propagation loss where the medians at 700 and 450 MHz are seen to be 13 and 7 dB higher than the median at 150 MHz, respectively.

The CDF of static RMS delay spread (calculated from a single impulse response) shown in Figure 2.5, indicate median values of 88 ns, at 150 and 450 MHz and 95 ns at 700 MHz. The probability of very large delay spreads, greater than 1200 ns is almost zero at 450 and 700 MHz, whereas it is non-zero at 150 MHz.

When comparing the propagation loss in outdoor-to-indoor environments at 1.8 GHz with those at 900 MHz, an extra 3 dB loss was found [RK12]. Furthermore, the distance from the building to the BS and the LoS conditions between them play an important role. When there is no direct LoS path, the power levels inside and around the buildings are more homogeneous and thus the fluctuations inside the buildings are less abrupt. This leads to the conclusion

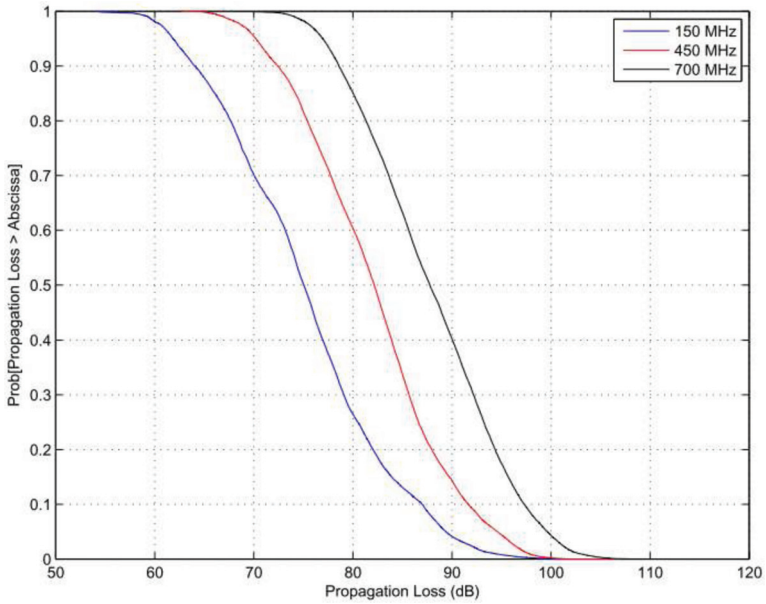

Figure 2.4 CCDFs for outdoor-to-indoor propagation measured in building 2 at CRC.

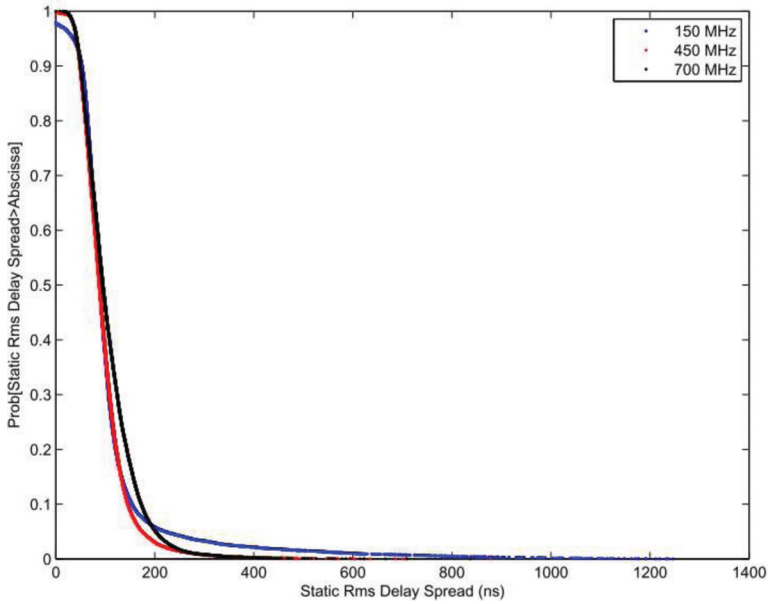

Figure 2.5 CCDF for static RMS delay spreads, estimated from all data measured in building 2 at CRC.

that even simple building models and less advanced indoor prediction models provide realistic assumptions on the coverage inside by means of empirical modelling. In the case when the BS is nearby and under LoS condition, a single path that follows the direct penetration line often has a dominant influence and thus results in a more inhomogeneous indoor coverage, which suggests the usefulness of using a semi-empirical model.

The indoor-to-outdoor propagation can be modelled using a hybrid model by combining two models: the extended angle-dependent multi-wall model, and the vertical knife-edge diffraction model. This can be done by modelling the effects on the direct propagation line (i.e., the penetration loss) between the femto-cell and the mobile terminal with a multi-wall model approach [COST231]. When the material parameters for the building are unavailable, empirical attenuation for different classes of walls can be used. Second, the diffraction loss can be modelled using the knife-edge diffraction model based on the elevation angles between the home-eNodeB, the window frame and the mobile terminal on the street. A hybrid-model that combines the dominant propagation effects from both models can be used by choosing the smaller PL of each. Thus the maximum received power from both predictions is achieved. This model provides good accuracy in the areas in front of the windows, but since only vertical diffraction is considered, the prediction is somewhat pessimistic in the areas on the left and on the right of the window [RJK12].

Vehicular-to-X

Different studies have been performed in order to evaluate the properties of vehicular-to-X channels and how these properties are affected by system parameters such as the position of antennas. These include vehicular-to-vehicular (V2V) and vehicular-to-infrastructure (V2I) in different propagation scenarios such as highway, urban, and rural.

The impact of antenna placement on V2V communications is analyzed in the work by Abbas et al. [AKT11]. Three propagation environments were chosen: highway, urban, and rural, where two Volvo V70 cars were used, each of which was provided with four omni-directional antennas, in azimuth, mounted at four different positions. The measurements were performed at a centre frequency of 5.6 GHz with 200 MHz bandwidth, where the TX and RX cars were moving in a convoy and in opposite directions. It was suggested that a pair of antennas with complementary properties, e.g., roof or left-side mirror mounted antenna together with a bumper antenna would reduce the shadowing on the RX antenna when vehicles are moving in opposite directions as shown in Figure 2.6.

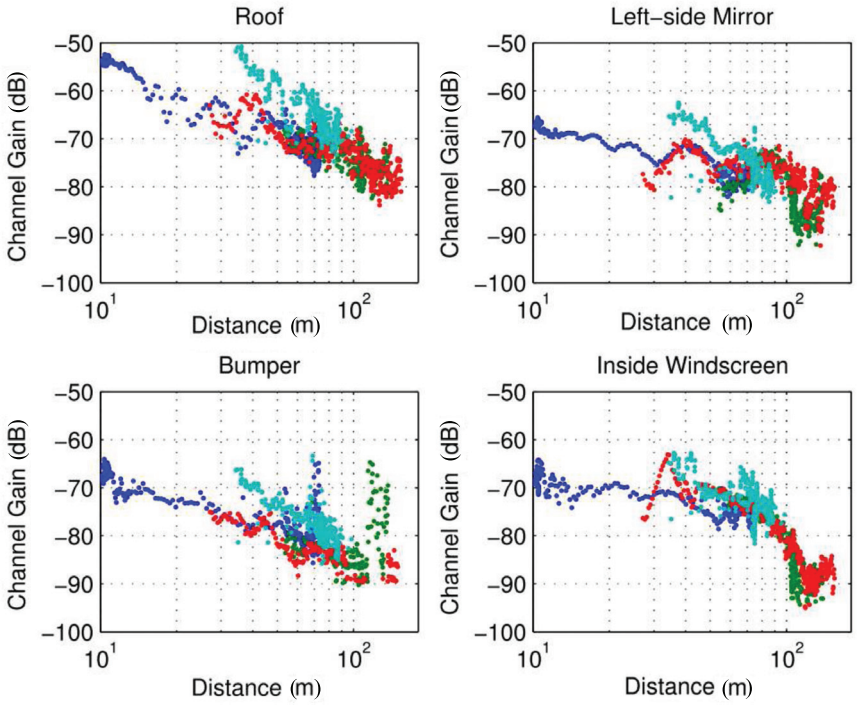

Figure 2.6 Measured channel gain for urban scenario when both vehicles were moving in a convoy. Results from four different measurements are shown with four different colours.

The influence of common shadowing objects like trucks on the wireless channel properties was addressed in Vlastaras et al. [Dim14], where a measurement campaign with a TX car incorporating six antennas and a RX car incorporating a single roof antenna was conducted. Two scenarios were considered; rural and highway. In both cases, a convoy formation was considered, where the TX was in the front, the RX was in the back and the truck was in the middle whenever present. See the different positions of the antennas in Figure 2.7.

The crucial rule of the antenna design, especially in regards of the radiation pattern of the MIMO antenna system for V2I communications was confirmed by Ekiz et al. [EKM12], where shadowing between the antennas found to cause a diminishing performance in areas close to the BS. It was pointed out that such effects can be circumvented by misalignment of the feed point of both antennas to obtain a radiation pattern being more congruent and closer to an omni-directional characteristic.

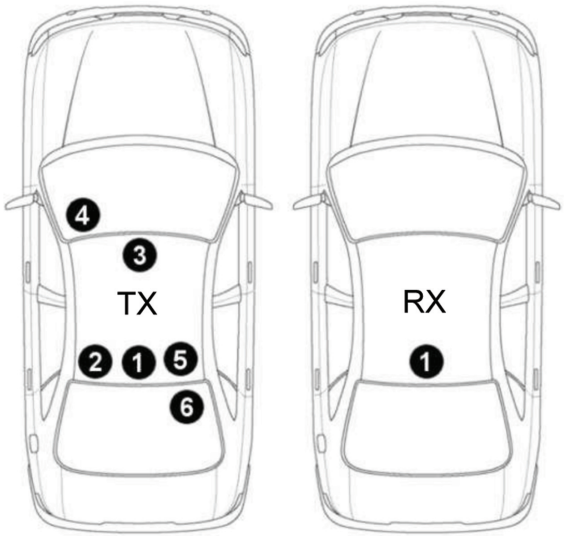

Figure 2.7 Antennas placement on the TX and RX cars. TX: Antennas 1, 2, 3, and 5 were omni-directional shark-n antennas mounted on the roof of the car. Antennas 4 and 6 were omni-directional antennas mounted inside of the front and rear windshields respectively. RX: A single omni-directional antenna was mounted on the roof of the car.

Hot-spots

A measurement campaign was performed in order to model radio channels with either LoS or NLoS connection between a UE and a NodeB in an operating universal mobile telecommunications system (UMTS). The statistics of the distance between the NodeB and the UE in LoS/NLoS scenarios, the life-distance of LoS channel, the LoS existence probability per location, and per NodeB, the power variation from LoS to NLoS transition and vice versa, as well as the transition duration were extracted [CYT+14].

Figure 2.8 depicts the empirical and fitted CDFs of the channel gains in the LoS and NLoS scenarios. It can be observed that the channel gains for LoS are concentrated in the region more to the right of the abscissa than the NLoS scenario. The results show that both CDFs are well fitted by normal distributions with parameters ($\mu = -90.68$ dB, $\sigma = 8.27$ dB) and ($\mu = -96.80$ dB, $\sigma = 12.92$ dB) for the LoS and the NLoS scenarios, respectively. It can be observed that the average of path loss PL for the LoS scenario is 6.12 dB higher than that in the NLoS scenario, and the STD of the channel gain in the LoS scenario is 4.65 dB less than that in the NLoS scenario. These statistical differences indicate that the existence of the LoS path in the channel

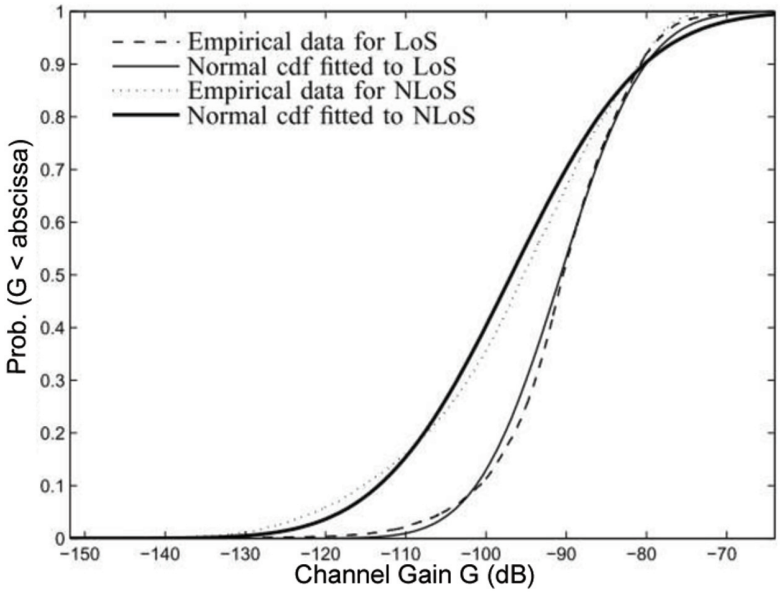

Figure 2.8 The empirical and fitted CDFs of the channel gains in the LoS and NLoS scenarios.

can not only bring 6 dB gain on average for the received signal, but also reduce the variation of the channel gain significantly.

Figure 2.9 illustrates the resultant probability density functions (PDFs) of direct distance from the NodeB to UE in LoS and NLoS scenarios, respectively. It can be observed that the NLoS users are at a maximum of 2.5 km, whereas the majority of the LoS users are located within 200 m from the NodeB. The NLoS users are widely spread within the range from 0 to 4 km, and the majority are within 300 m from the NodeBs. The non-zero probability observed for large range up to 4 km might be due to the existence of macro-cellular NodeBs. It was also found that the LoS and NLoS life-distances are usually less than 10 m, and the LoS-to-NLoS transition can be achieved in less than 10 ms.

2.1.1.2 Updated models in challenging conditions

Container terminals

In the work by Ambroziak and Katulski [AK13], the propagation loss based on the mobile, container, and terminal (MCT) model is compared to almost 290,000 measurements in a real container terminal environment. The obtained standard error of estimate (SEE) is 4.45 dB, which proves the accuracy and usefulness of the MCT model which may be used for frequencies from

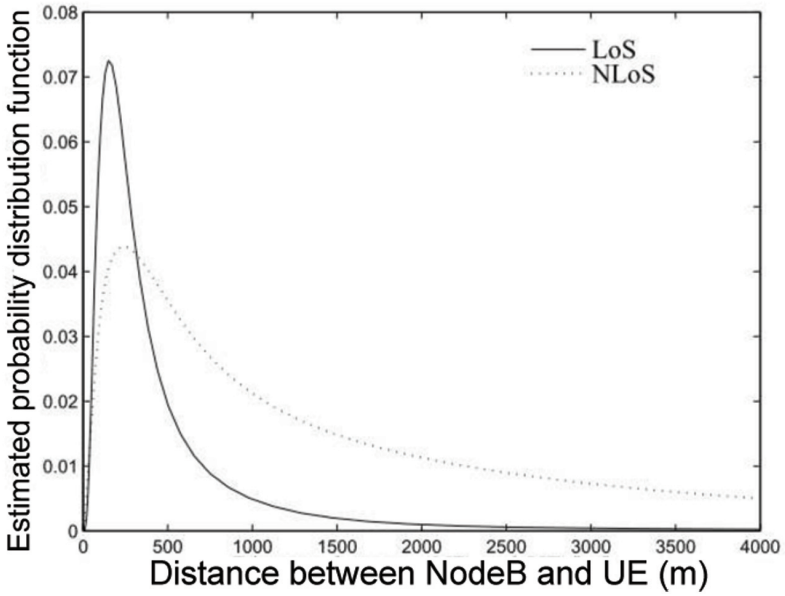

Figure 2.9 The empirical PDFs of the distance between the NodeB and the user equipment (UE) in LoS and NLoS scenarios.

500 MHz to 4 GHz, and path lengths from 50 to 620 m and BS antenna height between 12 and 36 m. The mean error (ME), and the SEE are listed in Table 2.1, where L_{LoS}, L_{Cont}, and L_{offT} are the PL for LoS, container area, and off-terminal area, respectively.

Rain

In order to investigate the effect of rain on attenuating the communication link in a wireless network, transformation of measured attenuation data available for long communication links to a hypothetical short link of 200 m length was applied in the work by Kantor et al. [KDB14]. Rain fading measurement data covering a span of 5 years were used assuming a carrier frequency of 38 GHz and horizontal polarisation. The attenuation on the hypothetical short link can then be calculated from Equation (2.3), where A_{r} (dB) is the

Table 2.1 Verification results of the MCT propagation model

Parameter	L_{LoS}	L_{cont}	L_{offT}	L_{mct}
ME (dB)	0.85	1.03	–0.26	0.72
SEE (dB)	4.40	4.53	4.30	4.45

attenuation on the real link that is exceeded with a probability $p = 0.01\%$ of the time, A_{h} is the attenuation on the hypothetical link, k_{r}, α_{r} (k_{h}, α_{h}) are frequency and polarisation-dependent empirical coefficients pertaining to the real (and hypothetical) links [ITU12], and r_{r} (r_{h}) is the distance factor of the real (hypothetical) link [ITU12].

$$A_{\mathrm{h}} = k_{\mathrm{h}} \cdot \left[\frac{A_{\mathrm{r}}}{k_{\mathrm{r}} d_{\mathrm{r}} r_{\mathrm{r}}} \right]^{\left(\frac{\alpha_{\mathrm{h}}}{\alpha_{\mathrm{r}}}\right)} d_{\mathrm{h}} r_{\mathrm{h}}. \tag{2.3}$$

The proposed transformation is adequate on $A_{0.01}$ (i.e., with $p = 0.01\%$); however, on different A_{p} values, the applicability of the proposed method has to be verified. Comparison of rain attenuation CCDFs of the reference link and of various hypothetical transformed links with the ITU theoretical curves, based on the $A_{0.01}$ values, is depicted in Figure 2.10. The transformed CCDFs and the ITU theoretical A_{p} curves for reduced path lengths are also nearly identical, except between exceedance probabilities of $p = 10^{-4}$ to $p = 10^{-6}$; however, this dissimilarity comes from the shape of the CCDF of the rain attenuation on the reference link. Therefore, it can be concluded that the proposed link transformation method is applicable on both short and long links since it takes the distribution of the rain intensity along the link path into account by considering the r distance factor as a constant for short ($<$250 m) path lengths.

In the work by Kntor et al. [KCD+14], the ratio of the disconnected nodes in a 5G microwave mesh network was investigated at high rain intensities in

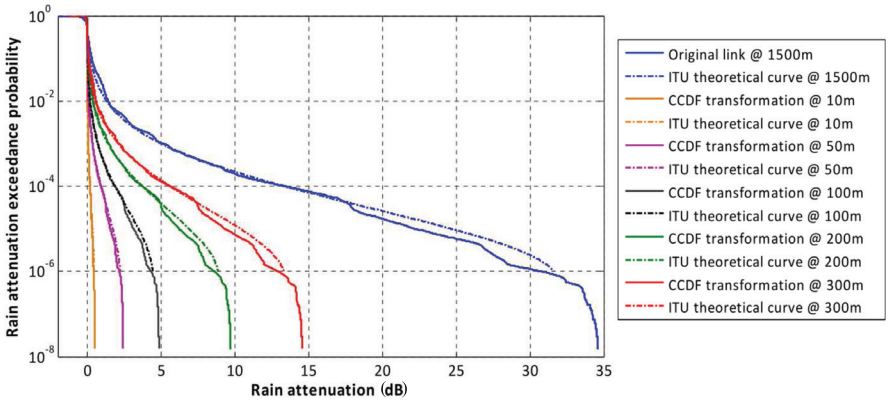

Figure 2.10 CCDF of the rain attenuation the transformed links according to the proposed method on different link lengths compared to the corresponding ITU theoretical curves based on $A_{0.01}$ (f = 38 GHz, pol = h).

a scenario when only rerouting is applied as a technique to improve network resilience. It was found that at high rain intensities (i.e., at low rain attenuation exceeding probabilities) the average ratio of the disconnected nodes can be considerable. Moreover, in a disadvantageous node deployment the effect of rain attenuation can be excessively harmful.

Vegetation

In the work by Torrico et al. [TCK12] and Chee et al. [CTK12], an analytical approach to compute the propagation loss for a typical mobile radio system in a vegetated residential area is discussed. In the described scenario, the transmitting antenna is elevated or around the average rooftop height, whereas the RX is located at street level and possesses no direct LoS to the TX. Using this approach, the total propagation loss Equation (2.4) is broken in three components, namely the free space loss, $\mathrm{FSL_{dB}}$, multi-screen diffraction loss, from the elevated transmitting antenna to the last screen adjacent to the mobile RX $L_{\mathrm{msd,dB}}$ and the rooftop-to-street diffraction loss combined with tree scaterring $L_{\mathrm{rts,dB}}$ [CTK12].

$$\mathrm{PL_{dB}} = \mathrm{FSL_{dB}} + L_{\mathrm{msd,dB}} + L_{\mathrm{rts,dB}}, \tag{2.4}$$

Train

Measurement campaigns between a high-speed train and a BS (i.e., a cellular deployment) were performed at 800 MHz, 930 MHz, and 2.6 GHz [Ke13, Flo14]. In the work by Guan et al. [GZAK13a], a semi-deterministic model for the propagation of high-speed railway was proposed, and it was found that the extended Hata model and multi-edge diffraction models can be conjunctively utilised to predict the PL in the viaduct and the cutting scenarios, which on average make-up more than 70% of the whole railway line. It was also found that the average estimated PL component is 3.2 and 3.5 dB at 800 MHz and 2.6 GHz, respectively which is in line with established PL models for rural areas [KBA+14].

2.1.1.3 Effects of user mobility, existence of pedestrians, and Tx/Rx antenna height

Effect of user mobility

The effect of arranging virtual sources of traced rays that arrive from the BS to the user in urban scenarios is addressed in Zentner et al. [ZMD12]. It was found that the common practice of placing virtual sources at the edges of the buildings where diffraction occurs yields correct results only for static

cases. When mobile users are considered, it results in the wrong estimate of Doppler shift. To overcome this problem, instead of locating the virtual sources at diffraction interaction points, it is suggested to set the virtual sources exclusively at a location that appears as a source to the mobile user [ZMD12].

To generate channel instances that take realistic user's movements inside a building into consideration, a two-step motion simulator was introduced in Rose et al. [RJHK13]. First, the motion between the rooms and the duration of time a user stays inside these rooms is calculated using a Markov jump process, which requires transition rates for each room to be stated in advance. These rates vary strongly depending on the time of the day and the type of building. Second, some spontaneous motion within the rooms is added to the simulation, such as: walking around, change position in the same room, walk back and forth between two positions, and visit another room (office) and come back to the original position. The last case represents a special case, since the non-spontaneous movement between rooms is determined in the first step.

These types of motion also vary highly with respect to daytime and the type of the building. Consequently, their associated probabilities are defined differently.

In the work done by Hahn et al. [HRSK15], a mobility model for simulating user mobility from indoor to outdoor and vice verse is introduced. The model simulates users moving from an entry point of a building to another based on real geographical data. The proposed model was compared with the well-known random walk mobility model. The comparison was conducted in the context of two prediction models: the extended Hata model and a complex 3D ray-optical propagation model. The results show that if a more advanced prediction model, e.g., the used ray-optical PL model, is applied, the use of a traditional random mobility model tends to produce results with more outliers towards lower and upper bounds.

Effect of existence of pedestrians

The effect of pedestrians on the properties of MIMO channels in small-cell setup was studied in Saito et al. [SIO14] based on measurements in the 2 GHz band. The measurements were carried out in a plaza of a typical urban railway station in Tokyo. To elucidate the influence of pedestrians on the channel properties, the measurements were carried out both in the daytime and at midnight. The height of the MS was fixed at 1.45 m, while two heights were considered for the BS, 1.45 m (L-scenario), and 2.9 m (H-scenario). As detailed in Table 2.2, the results indicate that in the day time, the received power and

Table 2.2 Large-scale parameters (LSPs) extracted from measurements for two BS heights 1.45 m (L-scenario), and 2.9 m (H-scenario), versus the ITU-RM2135 UMi (LoS)

Scenario		ITU-RM2135 UMi (LoS)	Measurement (H-scenario, Daytime)	Measurement (H-scenario, Midnight)	Measurement (L-scenario, Daytime)	Measurement (L-scenario, Midnight)
Delay spread (DS)	μ	–7.19 (65 ns)	–7.42 (38 ns)	–7.30 (50 ns)	–7.59 (26 ns)	–7.50 (32 ns)
Iog10 (s)	ρ	0.4	0.18	0.17	0.21	0.19
AoA azimuth spread	μ	1.75 (56°)	1.70 (50°)	1.73 (54°)	1.61 (41°)	1.62 (42°)
(ASAazm) log10 (°)	ρ	0.19	0.16	0.16	0.17	0.16
AoA elevation spread	μ		1.00 (10°)	0.91 (8°)	1.16 (14°)	1.07 (12°)
(ASAelv) log10 (°)	ρ		0.31	0.32	0.31	0.31
AoD azimuth spread	μ	1.2 (16°)	1.86 (72°)	1.85 (71°)	1.61 (41°)	1.62 (42°)
(ASDazm) log10 (°)	ρ	0.43	0.08	0.08	0.17	0.16
AoD elevation spread	μ		0.90 (8°)	0.88 (8°)	1.16 (14°)	1.07 (12°)
(ASDelv) log10 (°)	ρ		0.30	0.25	0.31	0.31
Cluster ASDazm (°)		3	5.6	6.0	5.3	5.2
Cluster ASDelv (°)			3.6	3.4	6.1	4.9
Cluster ASAazm (°)		17	5.9	6.0	5.3	5.2
Cluster ASAelv (°)			4.5	3.7	6.1	4.9

the delay spreads decreased, while the azimuth and angular spreads increased due to the change of propagation environment caused by the mobility and shadowing of pedestrians.

Effect of transmit/receive antenna height

The effect of BS height on LSPs was studied in the work by Böttcher et al. [Ann11] and Sommerkorn et al. [SKST12, SMS+14] based on several measurement campaigns at 2.53 GHz. In Böttcher et al. [BSVT11], antenna heights at 25 and 15 m at the BS were measured. It was found that under NLoS conditions, the delay-spread, K-factor and XPR significantly depend on the considered BS height and on the absolute distance to the mobile station. The DS was found to increase with increasing distance, while the K-factor and the XPR decrease as detailed in Tables 2.3–2.5.

In [SKST12] measurement with extremely elevated BS (approximately 118 m) were performed and the dependency of the LSPs on the elevation angle was confirmed, especially for the rms delay spread under NLoS conditions, where the average delay spread ranged from 72 ns to 151 ns (high to low elevation angle). Furthermore, the dependency of the LSPs on the elevation angle leads to the usefulness of sectorisation based on elevation beamforming as confirmed in [SMS+14].

For indoor environments, the effect of the height of the transmit and receive antenna on the delay spread was reported in the work by Salous et al. [SCR14], where the transmit antenna was placed either at 1.5 m or at the ceiling height and the receive antenna was either mounted on a trolley at 1.5 m or at the ceiling level at 2.6 m. Measurements were performed both in corridors and in offices. Table 2.6 summarises the results of the delay spreads in the different setups.

2.1.2 RT Techniques

For the 4G wireless communication system, the conventional semi-empirical or stochastic propagation prediction models are insufficient for network planning. Time dispersion and angular dispersion in a radio channel are important for the performance of the 4G network. The bandwidth of sub-carriers of OFDM system is determined by the knowledge of time dispersion in the radio channel. Moreover, smart antennas, consisting of adaptive array and MIMO antennas, are used for the 4G networks. Angular dispersion due to multipath propagation affects the spatial filter characteristics of the smart antennas and the effect is different for different kinds of smart antennas.

Table 2.3 Values for the mean and STD for the delay spread for different antenna heights and distance ranges

	NLoS		LoS	
	Mean (μs)	STD (μs)	Mean (μs)	STD (μs)
60–200m/25m	0.09	0.04	0.06	0.03
200–400m/25m	0.16	0.09	0.11	0.03
400–640m/25m	0.14	0.14	0.12	0.06
60–200m/15m	n.a.	n.a.	n.a.	n.a.
200–400m/15m	0.12	0.09	n.a.	n.a.
400–640m/15m	0.23	0.29	n.a.	n.a.

Table 2.4 Values for the mean and STD for the K-factor for different antenna heights and distance ranges

	NLoS		LoS	
	Mean (dB)	STD (dB)	Mean (dB)	STD (dB)
60–200m/25m	7.51	8.30	10.40	6.87
200–400m/25m	6.13	6.74	10.32	6.81
400–640m/25m	5.24	6.62	5.86	5.22
60–200m/15m	n.a.	n.a.	n.a.	n.a.
200–400m/15m	6.06 dB	7.47 dB	n.a.	n.a.
400–640m/15m	4.35 dB	6.55 dB	n.a.	n.a.

Table 2.5 Values for the mean and STD for the horizontal XPR for different antenna heights and distance ranges

	NLoS		LoS	
	Mean (dB)	STD (dB)	Mean (dB)	STD (dB)
60–200m/25m	8.09	5.33	7.63	4.66
200–400m/25m	7.40	3.62	11.63	3.67
400–640m/25m	3.87	2.88	6.96	2.52
60–200m/15m	n.a.	n.a.	n.a.	n.a.
200–400m/15m	6.10	2.83	n.a.	n.a.
400–640m/15m	2.79	2.77	n.a.	n.a.

Table 2.6 Summary of RMS delay spread obtained with different transmit and receive antenna height in indoor environment

	TX in Office with Antennas at Ceiling Height 2.6 m	TX in Corridor with Antennas at 1.5 m	TX in Office with Antennas at 1.5 m
Median value (ns)	11	18.53	13.74
90% value (ns)	12.5	25.16	20.15
10% value (ns)	8	8.49	10.74

For adaptive antenna arrays, angular dispersion degrades the performance of adaptive beamforming. However, for MIMO a wide angular spread of the multipath waves produces a large decorrelation of the spatial channels and hence increases diversity performance. The information of spread in angle domain and time domain cannot be predicted with the conventional empirical propagation models. Instead, deterministic prediction models become more interesting to predict the propagation channels for the 4G networks. The RT model is one of the popular deterministic models nowadays. It uses physical models of radio propagation mechanisms, such as reflection and diffraction, and detailed information of the environment to provide deep insight into the propagation channels. Most RT models with a detailed building database in urban scenarios results in excessive computational complexity, which limits the use by the mobile system operators. Most of the current research in the area of deterministic propagation modelling deals with reducing the computational complexity without losing the prediction accuracy, modelling effects like diffuse scattering or the use of efficient computational techniques to reduce time.

In this section, different uses of ray based techniques are shown, as a result of the work of different institutions in COST IC1004. From traditional approaches to improve computation time, to channel modelling or comparison with FDTD techniques, as well as just model simplifications for the 5G networks.

2.1.2.1 Diffuse scattering

The diffuse scattering phenomenon has been studied for years because of its relevance in the field of wave propagation and in many other fields of application as well (remote sensing, optics, physics, etc.), but its understanding is still far from being complete. It is well known that in the presence of smooth and homogeneous walls the basic interaction mechanisms can be analyzed using the geometrical optics approximation, thus all interactions are regarded as reflections, transmissions, and diffractions. Nevertheless, in a real propagation scenario the case of a perfectly smooth slab is rarely present, especially in dense urban areas where buildings have highly irregular structures and volume inhomogeneities: therefore, modelling only specular and transmitted paths might not be sufficient because of the presence of the so-called dense multi-path component (DMC), which have a significant impact on the radio link, especially in the case of NLoS propagation [LMV14].

In the work by Vitucci et al. [LTY14] a semi-deterministic propagation graph modelling approach is proposed based on the framework of graph

theory. Unlike in the original stochastic propagation graph modelling, the graph in our method is set up by the aid of digital maps: walls and buildings are discretised into scatterers whose spatial distribution over planes or volumes reflect the shape of the actual obstacle they represent. Scatterer distribution and corresponding propagation coefficients are jointly defined in order to satisfy realistic propagation conditions, such as the power-distance decay law, power balance, transmission attenuation, etc. The proposed model is very suitable for highly diffuse scattering conditions, such as propagation at mm-wave and terahertz frequencies.

Some works in the diffuse scattering issue, by Vitucci et al. [EVC11] and Mani and Oestges [MO12], were evolving from the effect of smooth walls to the introduction of the effect of trees, trying to demonstrate the accuracy of the model, where simulations taking into account LoS propagation, reflection, diffraction, and diffuse scattering were tested.

In the work by Oesteges [Oes14], a measurement campaign to verify diffuse scattering in 12.5 and 30 GHz is described. This paper analyzes some limitations of the diffuse approach.

2.1.2.2 RT in vehicular networks

The evolution of vehicular networks led to the development of improved RT-based models to vehicular environments. Several works around the use of ray-based techniques in vehicular environments were proposed along the IC1004. Mainly, works by [JNK12], Werthmann et al. [TJT12], and Rose and Kürner [RK14] were devoted to the use of ray-based in vehicular environments.

RT for vehicular networks includes three major wave propagation mechanisms: (i) LoS, (ii) specular components, as well as (iii) diffuse scattering. It relies on the calculation of all propagation paths connecting the TX and the RX location for a given propagation mechanism. The RT channel model enables the calculation of the electric field in amplitude, phase and polarisation at the mobile terminal position.

As a deterministic channel model in the work by Werthmann et al. [TJT12], authors propose the use of a 3D ray-optical model that has initially been developed for car-to-car communication purposes. The model has been extended by a diffraction model for the development of the Hanover 3D reference scenario. The following types of rays are considered in the model: direct path, specular reflections up to *n*th order (2nd order in this case), diffuse scattering, and diffraction. The direct path between the TX and RX is identified by a LoS check using 3D polygons of the buildings of Hanover. The specular reflections are calculated based on the image method (RT). Due to the high

computation time only 2nd order reflections are considered. On surfaces seen by both the TX and RX diffuse scattering is taken into account. Diffraction is considered using the knife edge model shows an example of the identified rays between the TX on a rooftop of a building and RX located on the street level.

The underlying simulation-based channel model that is used in the work by Nuckelt et al. [JNK12] belongs to the class of deterministic channel modelling approaches using 3D ray-optical algorithms. In order to characterise the channel between TX and RX, the direct path, specular reflections, as well as diffuse scattering in terms of non-specular reflections are taken into account. Specular reflections are calculated recursively up to a desired order, but depending on the complexity and level of detail of the environment only reflections up to order three or four are practical regarding computational effort. Faces of buildings or obstacles that can be seen by both the TX and the RX are treated as sources of non-specular reflections of first order, modelled by means of Lambertian emitters. Furthermore, the channel model is able to include the full-polarimetric antenna patterns of TX and RX, respectively.

2.1.2.3 Channel modelling for 5G networks

During the last years, the use of Ray Based techniques for channel modelling has been evolving, and during the COST IC1004, many works related with this issue were presented and different approaches were proposed. In the work by Zenter et al. [ZK13, ZH14, RZD12], the concept of a virtual source for deterministic reference channel models (RCMs) is introduced and developed. The feasible option for geometry-based RCM would be a set of RT-simulated environments. RT allows high-resolution simulations, thus providing a very detailed description of the radio environment and the propagation phenomena. The concept of ray entity reduces the computational complexity for RCMs in complex scenarios.

Kaltenberger et al. [MT13] propose the use of RT based on a spheroidal subspace, as a deterministic technique which is currently employed to predict wireless channel parameters such as delay spread, Doppler spread, and angular spread in a variety of environments and a wide range of frequency. The multipath channel model is the representation of complex phenomena involving several mechanisms of interaction between the radio wave and the environment. Accordingly, through spatial and time characterisation it is possible to design and theoretically evaluate the wireless communication

systems. Time variant channel impulse response can be seen as a superposition of all propagation paths' contributions, which can be calculated as:

$$H_{\mathrm{RT}}(f, x(t)) = n = 1]N \sum \eta_{\mathrm{n}}(x(t)) e^{j2\pi f T_{\mathrm{n}}(x(t))} \tag{2.5}$$

where *n* is the propagation path index, $\eta(x(t))$ is the complex-valued weighting coefficient of the n_{th} path, $T_n(x(t))$ is the delay, and N is the total number of paths.

In the work by Vitucci et al. [EVE14], the authors show the use of ray-launching techniques for channel modelling in large indoor environments, showing the restrictions presented when detailed information about the scenario is not present. This work compares simulating results with measurements in order to identify the elements required for an accurate modelling of the scenario.

Garcia-Pardo et al. [JPGLL] discuss a PDP estimation using a ray-launching tool implemented in Matlab, and compare results with measurements in 60 GHz band. In this work the authors implement diffuse scattering, based on the works described above.

In the work by Kitao et al. [NO15], the authors propose alternative model for buildings at the intersection to improve the accuracy of RT calculation. Specifically, the conventional model assumes box-shape as a building while the proposed model considers more detailed shape of building. The proposed and conventional models are used in RT calculation, respectively, and the accuracy is evaluated.

The approach of Baek et al. [SHP14a, SHP14b] is based on a simplification of a propagation model and channel estimation procedures using ray-based simulations to obtain slope parameters and cluster information, in order to accelerate simulations results for real implementations in the 5G networks.

For wideband channels, like those used in long-term evolution (LTE)-A and ultra wideband (UWB) networks, Gan et al. [PW13] uses the concept of simulating the propagation channels at multiple frequency points, which are the centre frequencies of the corresponding subbands. The accuracy of the subband divided RT is related to the number of the sub-bands: the larger this number the better the accuracy, but at the cost of a higher computational effort. Subband divided RT can be summarised with the following steps:

- The whole UWB bandwidth is divided into several subbands. In each subband, constant frequency characteristics can be assumed for all materials and mechanisms.

- Conventional RT is used to obtain the channel impulse response (CIR) at each sub-band centre frequency.
- The subband frequency responses are calculated by Fourier transforms. Afterwards all frequency responses over different subbands are combined into a complete frequency response over the whole UWB bandwidth.
- Finally, the CIR over the entire UWB bandwidth can be obtained by an inverse Fourier transform.

The complete frequency response can be expressed as:

$$H(f) = [i = 1]N \sum F\{h_i(T) \cdot R_i(f)\}, \tag{2.6}$$

where i is the sub-band index, N is the total number of subbands, $F\{\cdot\}$ is the Fourier transform, $h_i()$ is the CIR at the ith sub-band, and $R_i(f)$ is the rectangular window function associated with the ith sub-band.

2.1.2.4 Improvements of ray launching

It is well known that RT models are deterministic and, therefore, it is expected a very precise prediction for radio propagation. However, such models require information of material's constitutive parameters, increasing the difficulty of use because of the absence of such parameters. This is especially true in outdoor environments, because the diversity and quantity of building blocks typically found in outdoor environments. Although some works have been done trying to obtain constitutive parameters for different materials and building blocks, the diversity is such that it is almost impossible to characterise all possible environments. This is a major constraint related with the accuracy of RT methods, that is usually solved using some typical values for constitutive parameters, according to the environment. In Navarro et al. [DGC13], the problem of parameters calibration is discussed and some techniques to improve computational time are proposed.

In the work by Pascual-Garcia [MMIJL12], a 3D RT technique which has been fully programmed in Matlab was applied to calculate most important channel parameters. The mentioned method is based on image theory. Images of the TX are computed for each wall, and then reflections are considered if the ray hits the corresponding wall. This software is programmed to compute any order of reflection. The diffraction phenomena is also considered, and the software searches all wedges, and it also finds the images of the TX and RX (diffraction + reflection). The position of each image depends on the scenario element position where the reflection takes place. Therefore, the accuracy of

the RT technique relies on the precision of the 3D model of the real scenario. In this work, special care has been taken in the definition of the 3D model.

In Andersen et al. [SFF12] simulations of free-space propagation and rooftop diffraction using the FDTD method and RT method are described and compared. Concerning the free-space propagation simulations, the two methods show similar results. However, the FDTD computation time is much larger than the RT one, demonstrate the importance of improving the ray-based algorithms for better propagation and channel estimation.

Vitucci et al. [EVB15] discusses the precision of RT models for traditional propagation signal losses estimation using a set of measurements in cities like San Francisco and the sensitivity of ray based models to the simulated scenario versus the real scenario.

Finally, Brem et al. [MME13] proposes a modification of the wave front to improve accuracy of RT in conditions where far field is not guaranteed. This approach simplifies the mathematical model and reduces the computation time.

2.1.3 Massive and Distributed MIMO

In this section we present recent advances in the topic of channel modelling for massive and distributed MIMO.

2.1.3.1 Massive MIMO

Massive MIMO is an emerging communication technology promising order-of-magnitude improvements in data TP, link reliability and transmit energy efficiency [Mar10, RPL+13, LTEM14, NLM13]. This approach involves multi-user MIMO (MU-MIMO) operation with an arbitrarily large number of BS antennas in a multi-cell environment. It is shown that, under these operating conditions, the effects of uncorrelated noise and fast fading disappear, as does the intra-cell interference, and the only remaining impediment is the inter-cell interference due to pilot contamination. In this regime, simple matched filtering (MF) linear pre-coding becomes optimal and capacity can be achieved with relatively inexpensive signal processing.

The fundamental idea of massive MIMO is that, as the number of BS antennas grows large, the channel vectors between users at the BS become pair-wise orthogonal. This ideal situation is often referred to as “favourable” propagation conditions. Experimental work is, therefore, of great importance to investigate the range of validity of this assumption: what benefits can we obtain at very large, but limited, number of BS antennas in a realistic scenario?

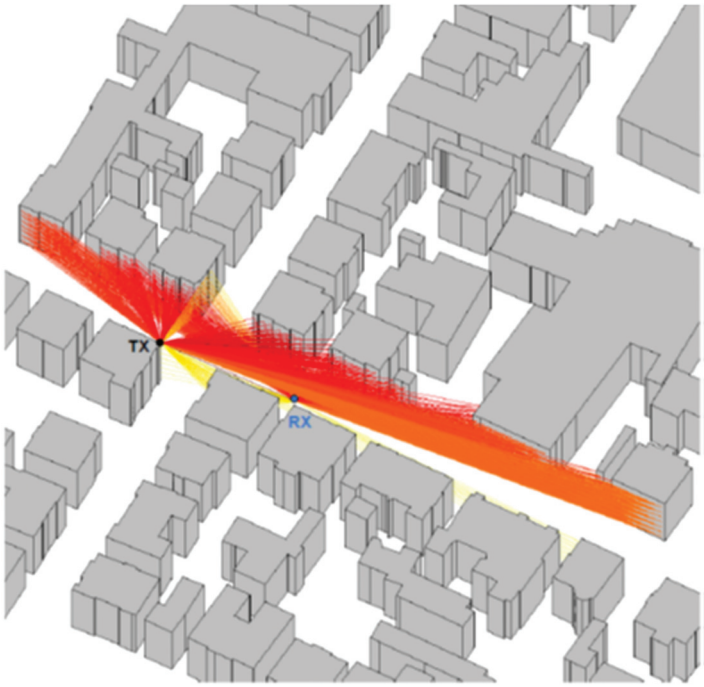

Figure 2.11 3D Rays in Hannover scenario.

In an effort to answer this question, measurements were conducted in a residential area north of Lund, Sweden, representative of a suburban environment [GERT11]. The BS array was placed indoor, while the user terminals were located at different outdoor positions with similar LoS directions to the BS. The array is a cylindrical antenna array with 64 dual-polarised antenna elements, giving in total 128 antenna ports (Table 2.7). The measurement data were recorded with the RUSK LUND channel sounder [THR+00] using a centre frequency of 2.6 GHz and a measurement bandwidth of 50 MHz. Some results on the sum-rates achievable by zero forcing (ZF) and minimum mean-squared error (MMSE) linear pre-coding schemes with random antenna selection are shown in Figure 2.11, for the case of two users being served. Clearly, the average correlation between the users' channels decreases as the number of antennas[1] at the BS increases. This suggests that practical very-large arrays can decorrelate multi-user channels

[1]Whenever there is no risk of confusion, we will use the shorter term "antenna" in place of "antenna port".

Table 2.7 Comparison of two large antenna arrays at the BS side

Cylindrical	Linear
128 antenna ports	128 antenna ports
Compact array (30 cm × 30 cm)	Physically-large array (7.3 m)
Two-dimensional	One-dimensional
Multiplexed	Virtual
Dual polarised	Single polarised
Directional elements	Omni-directional elements
Resolution in 2D	Superior (1D) angular resolution

in realistic propagation scenarios. Indeed, with as few as 20 BS antennas, the linear pre-coding sum-rates already reach 98% of the dirty-paper coding (DPC) capacity (Figure 2.12b). Similar conclusions are reached in Flordelis et al. [FGD+15], where results on the ability of massive MIMO systems to spatially separate eight users located close to each other in an outdoor environment with LoS to the BS are reported. These capacity/sum-rate results reinforce previous findings in the related literature that a large fraction of the predicted capacity gains of very-large MIMO are possible at sizes of the BS array as low as 10 times the number of users served.

The impact of the shape and size of the BS antenna array on the performance of massive MIMO systems is discussed in [GTER13]. Several considerations apply when selecting the form factor of very-large antenna arrays. For instance, from a practical point of view, it is preferable to have a physically-compact array with a large number of antennas at the BS. On the other hand, making the arrays smaller in size brings about some drawbacks such as higher antenna correlations. In [GTER13], the performances achievable using a 128-element cylindrical array and a 128-element linear array in realistic propagation environments are compared. The main properties of the BS antenna arrays used in this study are summarised in Table 2.7. Channel measurements were performed in a suburban environment, at the Faculty of Engineering (LTH) at Lund University, Lund, Sweden. The two BS antenna arrays were placed on the same roof. More precisely, the cylindrical array was positioned on the same line as the linear array, near its beginning. Both measurement data sets were recorded using a centre frequency of 2.6 GHz and a measurement bandwidth of 50 MHz. An omni-directional antenna was used at the user side.

It is observed that, under random antenna selection, the variations incapacity/sum-rate experienced by the cylindrical array are larger than those experienced by the linear array. In the same way, the average capacity/sum-rate offered by the linear array tends to be higher than the average capacity/sum-rate

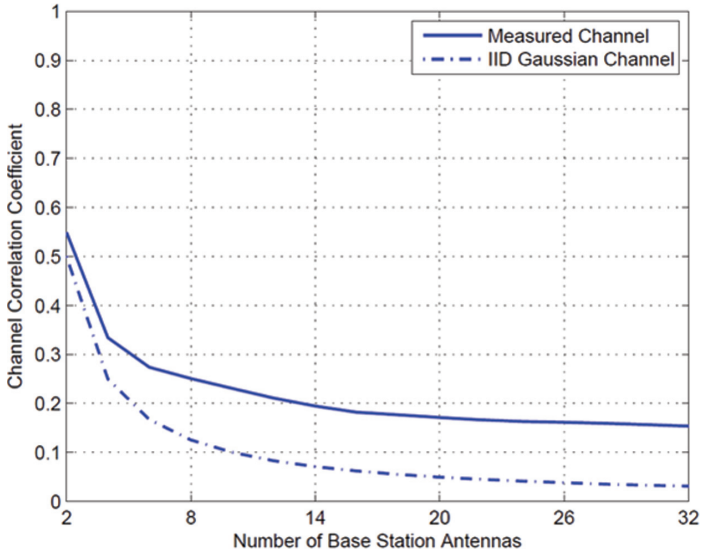

(a)

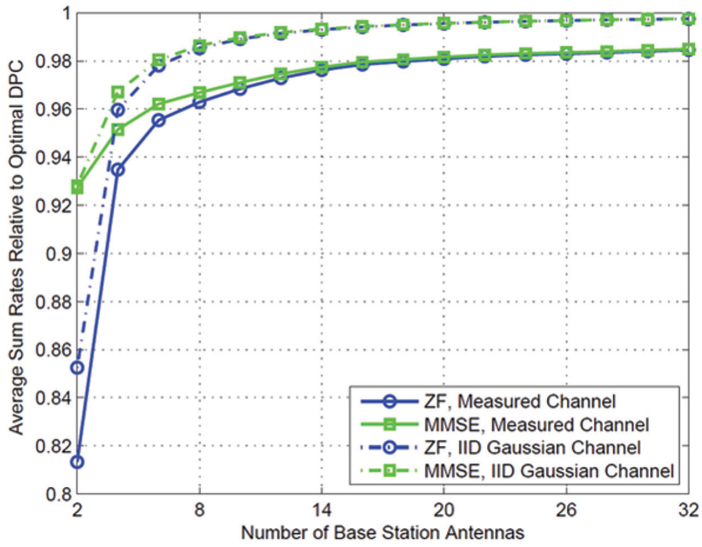

(b)

Figure 2.12 Average channel correlation (a) and ratio of average linear pre-coding sum-rate and DPC capacity (b) as a function of the number of BS antennas. The transmit signal-to-noise-ratio (SNR) is set to 20 dB and the total transmit power is kept unchanged.

at the cylindrical array. One possible explanation is that the variations induced by the polarisation and directionality characteristics of the antenna elements of the cylindrical array (the antenna elements of the cylindrical array are directional, dual-polarised patches, while the linear array is virtually formed by an omni-directional, single-polarised antenna element, (see Table 2.7) seem to have a larger impact on capacity/sum-rate than the large-scale fading (LSF) along the linear array caused by the environment where the measurements are performed (and assumed negligible for physically compact arrays).

The presence of LSF across the antenna elements of a physically large antenna array was noted in the work by Payami and Tufvesson [PT12]. The most important observation is that the channel cannot be seen as wide-sense stationary over the physically-large array. This situation is illustrated in Figure 2.13, which shows the angular power spectrum over a BS physically large antenna array for a user location with NLoS [GTER12, GZT$^+$15]. Cluster parameters according to the COST 2100 channel model have been extracted following Czink et al. [CCS$^+$06] and Czink [Czi07], and are also shown in Figure 2.13b. We note that some scatterers are not visible over the whole array and, for scatterers being visible over the whole array, their power contribution varies considerably. This power variation may be critical to algorithm design and performance evaluation of very-large MIMO systems. Therefore, it is important to model the LSF process over physically large arrays. The modelling approach attempted can be seen as an extension of the COST 2100 channel model [VZ12], in which only small and compact multiple antenna arrays are considered. In the work by Gao et al. [GTER12, GZT$^+$15], the concept of cluster visibility region (VR) in the COST 2100 channel model is proposed to be used at the BS side, as well, to account for LSF over physically-large antenna arrays. At the mobile side, the VR concept is used without changes. This concept is illustrated in Figure 2.14. Now, for the propagation link between a BS antenna element and a MS, a cluster is active when the antenna element is inside the cluster's BS-VR *and* the MS is inside the corresponding MS-VR. Both conditions should be satisfied to declare a cluster being active.

Some new parameters are added to the COST 2100 channel model to account for the BS-VR model extension. These are:

- The total number of clusters that are visible over a physically large array.
- As can be seen from Figure 2.14, more clusters are visible for a physically-large array as compared to a compact array and so, the total number of clusters in the conventional model is not suitable any more.

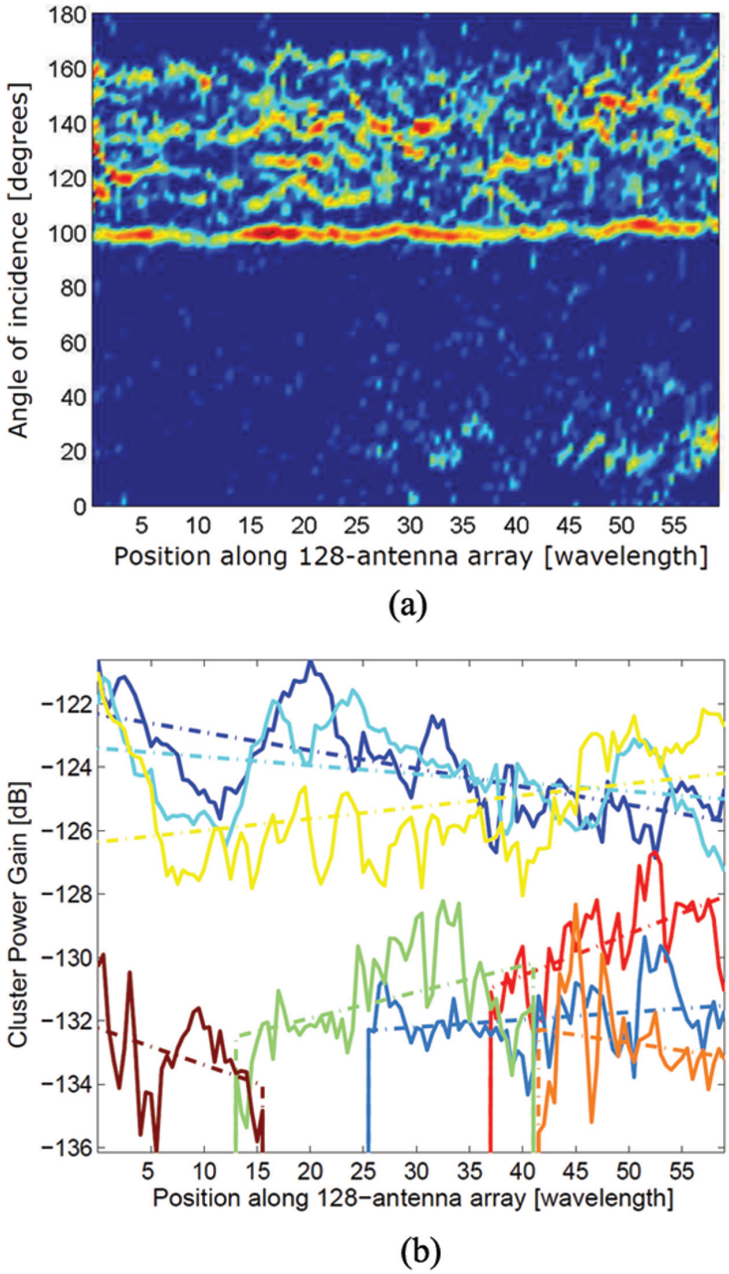

Figure 2.13 Angular power spectrum over the BS antenna linear array (a) and cluster power variation with least square linear fitting (b). The user is located at a position with NLoS.

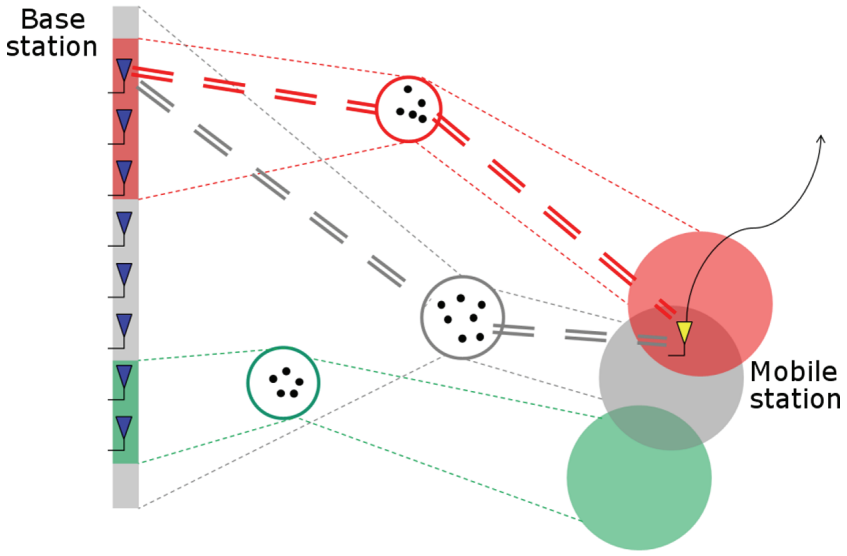

Figure 2.14 Extension of the concept of cluster VR to the BS side. The clusters in *red* and *grey* colours are active.

- The shape and size of BS-VR. For example, the BS-VRs of physically large linear arrays are modelled in the work by Gao et al. [GZT+15] as intervals on a line, rather than circular regions as those used for modelling the MS-VRs.
- Cluster power variations within BS-VR. It is found appropriate to replace the cluster visibility *gain function,* which describes the time evolution of clusters at the user side, by a slope—the cluster visibility *gain,* which characterises the power variation of those clusters visible at the BS side across the antenna array elements.

A detailed description of the modelling and parameterisation of BS-VRs for a physically-large antenna array in NLoS propagation conditions can be found in the work by Gao et al. [GTER12, GZT+15]. The modelling of MS-VRs in the conventional model cannot be directly applied to BS-VRs since MS and BS usually have very different propagation environments in their vicinity.

2.1.3.2 Distributed MIMO

Spatially distributed MIMO antenna systems, also known as coordinated multi-point (CoMP) or distributed MIMO, is a novel communication technology that aims at improving spectral efficiency and fairness for wireless mobile

communication networks [MF11]. The main idea behind distributed MIMO systems is that deploying the antennas of the BSs over a large geographical area should increase the probability of a MS of experiencing high signal strength conditions on one or more *links,* simultaneously. Of course, this idea rests on the assumption that different links undergo independent LSF and, hence, the achievable gains of a distributed antenna system will ultimately depend on the correlation properties of the so-called LSPs of the links, such as LSF (F), delay spread (τ_{rms}), azimuth angular spread (ϕ_{rms}) and elevation angular spread (θ_{rms}). Correlation between LSPs belonging to different links is often explained by the existence of interacting objects (IOs) common to those links and, in this sense, it is environment specific.

In Dahman et al. [DFT13, DFT14], multi-site, fully-coherent measurements conducted with the RUSK LUND [THR$^+$00] channel sounder using a centre frequency of 2.6 GHz and with a measurement bandwidth of 40 MHz are reported. The measurement campaign took place at the Faculty of Engineering (LTH) at Lund University, Lund, Sweden, in a suburban environment with low buildings, rich vegetation, and a small pond at the centre. The setup chosen consists of four single-antenna BSs communicating with a MS provided with a 128 antenna ports array as described in Section 1.1.1. The BS antennas were placed outside the windows at the second and third floors of four different buildings, which corresponds to 5–12 m above the ground level and 10–20 m below the surrounding buildings. The distance between antenna sites varies between 60 and 200 m. BS antennas are connected to the channel sounder device by means of RoF links. A photo of the measurement area with the positions of the BSs can be seen in Figure 2.15. During the measurements, the MS circulated the pond counter-clockwise at pedestrian speed (less than 0.5 m/s) along a predefined route with a length of 490 m. The propagation conditions over the whole route can be described as obstructed line-of-sight (OLoS) due to the presence of high, leafy trees in the measurement area blocking the LoS from the MS to the BSs. The intensity of the tree blockage varies from one MS position to another. It must be noted, however, that the probability of having LoS between the MS and one of the BSs is significant when the MS is close to that BS.

Details about the extraction of the LSPs can be found in [DFT13, DFT14]. Following a methodology similar to that introduced in the work by Kyösti et al. [KMH$^+$08], we make use of the Box–Cox transformation in order to transform non-normally distributed LSPs to another domain where they have approximately normal distributions. Then, in the transformed domain, we estimate the parameters of the corresponding Gaussian distributions of the

Figure 2.15 Aerial photograph of the measurement area. BSs locations are indicated by labels BS-E, BS-S, BS-F and BS-M. The measurement route is plotted in *blue* colour.

LSPs and the correlation coefficients between LSPs. The Box–Cox transform with *power parameter* is defined as

$$g(x)^{(\lambda)} = \begin{cases} \frac{x^{\lambda}-1}{\lambda}, & \lambda \neq 0 \\ \log(x) & \lambda = 0. \end{cases} \tag{2.7}$$

For each LSP and each BS, we choose the value leading to the distribution in the transformed domain that is closest to normality. The transformed delay spread, angular azimuth spread and angular elevation spread are denoted by $g(\tau_{\mathrm{rms}})$, $g(\phi_{\mathrm{rms}})$, and $g(\theta_{\mathrm{rms}})$, respectively, and their corresponding Box-Cox power parameters by λ_{τ}, λ_{ϕ}, and λ_{θ}. We note that $\lambda_{\phi} = 0$ and, therefore, it follows that $g(F) = F$. Tables with the fitted Box–Cox power parameters can be found in the work by Dahman et al. [DFT14a]. From the estimates of the LSPs obtained as described above, we then estimate the auto-correlation functions of the LSPs and the correlation coefficients of LSPs belonging to the same link (*intra-link* correlation coefficients) and to different links (*inter-link* correlation coefficients).

We first consider the LSPs belonging to the whole measurement route at once for estimating the auto-correlation functions and intra- and interlink correlation coefficients. We refer to this case as *global-scale* LSPs. The following remarks, which are in good agreement with reports available in the existing literature, can be made:

- The value of the auto-correlation distance[2] of the same LSP varies significantly from one link to another. See the work by Dahman et al. [DFT14a] for further details.
- For the intra-link case, there is a significant negative correlation between F and $g(\tau_{\mathrm{rms}})$, for all links. In general, F is negatively correlated with the rest of the (transformed) LSPs.
- For the intra-link case, there is a positive correlation between $g(\phi_{\mathrm{rms}})$ and both $g(\tau_{\mathrm{rms}})$ and $g(\theta_{\mathrm{rms}})$.
- Values of the correlation coefficients for global-scale, inter-link LSPs fall in the range ± 0.44. In general, inter-link LSPs display lower values of the correlation coefficient than corresponding intra-link LSPs.

The low values of the correlation coefficients of the inter-link LSPs found at the global-scale may suggest the viability of ignoring inter-link correlations when simulating multi-link systems. However, one should remember that these small values of the estimated global-scale inter-link correlation coefficients are obtained by considering the whole measurement route at once, a length of 490 m, which might exceed the extension of the joint stationarity region of the multi-link LSPs. Simulations of wireless channels are often performed as a series of *simulation drops,* each of which is between few meters to few tens of meters long, and each simulation drop is assumed to have constant LSPs. Therefore, it will be valuable to utilise our measurements in order to extract a model that describes the correlation coefficients among the LSPs of the different links at a *local-scale*, i.e., within short parts of the route of ten to few tens of metres length.

The use of the truncated Gaussian distribution, TG(μ, σ^2), to model both the intra- and inter-link correlation coefficients of the LSPs on the local-scale is proposed in the work by Dahman et al. [DFT14a]. The model can be used as follows:

1. Depending on the LSPs considered and on the intra-link or inter-link case, use Tables 2.8, 2.9, or 2.10 to generate values for $\mu \sim u(\mu_{\min}, \mu_{\max})$ and

[2]The *auto-correlation distance* is defined as the distance at which the magnitude of the auto-correlation function has decreased to e^{-1} of its peak value.

Table 2.8 Local-scale inter-link correlation coefficients (same LSPs)

	F	$g(\tau_{\mathrm{rms}})$	$g(\phi_{\mathrm{rms}})$	$g(\theta_{\mathrm{rms}})$
$\mu_{\min}$	–0.25	–0.18	–0.16	–0.10
$\mu_{\max}$	0.28	0.33	0.23	0.28
$\sigma_{\min}$	0.23	0.23	0.28	0.14
$\sigma_{\max}$	0.52	0.47	0.39	0.39

Table 2.9 Local-scale inter-link correlation coefficients (different LSPs)

	F, $g(\tau_{\mathrm{rms}})$	F, $g(\phi_{\mathrm{rms}})$	F, $g(\theta_{\mathrm{rms}})$	$g(\tau_{\mathrm{rms}})$, $g(\tau_{\mathrm{rms}})$	$g(\tau_{\mathrm{rms}})$, $g(\phi_{\mathrm{rms}})$	$g(\phi_{\mathrm{rms}})$, $g(\theta_{\mathrm{rms}})$
$\mu_{\min}$	–0.31	–0.28	–0.26	–0.17	–0.17	–0.11
$\mu_{\max}$	0.21	0.18	0.19	0.33	0.25	0.29
$\sigma_{\min}$	0.24	0.20	0.20	0.20	0.18	0.17
$\sigma_{\max}$	0.61	0.55	0.52	0.50	0.50	0.42

Table 2.10 Local-scale intra-link correlation coefficients

	F, $g(\tau_{\mathrm{rms}})$	F, $g(\phi_{\mathrm{rms}})$	F, $g(\theta_{\mathrm{rms}})$	$g(\tau_{\mathrm{rms}})$, $g(\tau_{\mathrm{rms}})$	$g(\tau_{\mathrm{rms}})$, $g(\phi_{\mathrm{rms}})$	$g(\phi_{\mathrm{rms}})$, $g(\theta_{\mathrm{rms}})$
$\mu_{\min}$	–2.50	–2.50	–2.24	0.68	0.32	0.54
$\mu_{\max}$	–0.82	–0.58	–0.41	2.50	1.67	2.50
$\sigma_{\min}$	0.09	0.10	0.26	0.08	0.26	0.19
$\sigma_{\max}$	0.89	1.00	0.80	0.91	0.80	0.80

$\sigma \sim u(\sigma_{\min}, \sigma_{\max})$, where $u(a, b)$ represents a uniform distribution in the interval [a, b].

2. Generate $r \sim G(\mu, \sigma^2)$, where $G(\mu, \sigma^2)$ represents a Gaussian distribution with mean μ, and variance σ^2.
3. Repeat step 2 while $|\rho| > 1$.
4. Repeat steps 2 and 3 for each simulation drop.

The proposed method can indeed reproduce the large variability exhibited by the correlation coefficients on the local-scale. For example, if $\mu = -0.31$ and $\sigma = 0.14$ are used to model the inter-link correlation coefficient of one link pair, then the corresponding probability of having $\rho > 0.5$ is almost zero. However, for another simulated link pair, if $\mu = 0.33$ and $\sigma = 0.61$ are assumed, then the probability of having $\rho > 0.5$ will be 0.30. Performing step 1 only once guarantees that the values of the correlation coefficients are consistently generated over a whole batch of simulation drops since, for each LSP, its mean and variance remain unchanged. A further simplification of the model is possible if one observes that, for any pair of LSPs, the results reported in Tables 2.8 and 2.9 can be approximated by drawing μ and σ from uniform

distributions in the intervals [–0.31, 0.33] and [0.14, 0.61], respectively (step 1).

It should be noted that, despite the fact that the parameters in Tables 2.8, 2.9, and 2.10 correspond to a Gaussian model, depending on the selected pair of parameters (i.e, μ and σ), the actual resulting distributions after truncation might have shapes not resembling that of a Gaussian distribution. For example, selecting ($\mu = -2.5$, $\sigma = 1$), ($\mu = 2.5$, $\sigma = 1$), and ($\mu = 0$, $\sigma = 1$) will result in PDFs that look like exponential PDF, truncated bell shape PDF, and reverse exponential PDF, respectively.

On a related topic, fully coherent measurements of a multi-link setup in which the antenna elements of the BS are separated up to several metres are reported in the work by Dahman et al. [DFT15], with a discussion of further extensions to the COST 2100 channel model to accurately describe radio propagation in this scenario.

2.1.4 Cellular mm-Wave

Mobile data traffic is projected to grow 5000-fold by the year 2030. This drastic increase can only be met through increase in performance, spectrum availability and massive network densification (small cells). The availability of large contiguous blocks of spectrum in the mm-wave band (30–90 GHz) could be exploited to enable very significant (1 GHz or more) increase in bandwidth in cellular communication systems. Also, at these higher frequencies, antenna elements are smaller which enables the implementation of large array antennas for beam forming to compensate for propagation losses, and to achieve significant system capacity and TP gains [RSP+14, PK11, RSM+13]. Having access to such large blocks of spectrum also makes possible in early deployments to trade-off spectral efficiency for bandwidth, i.e., high-data rates can be achieved even with low-order modulation schemes requiring lower powers and lower complexity and cost. To enable the development of next generation mobile systems, it is of utmost importance to characterise mm-wave propagation in small cell scenarios and to develop accurate channel models. Significant challenges arise with regard to channel sounder hardware development, channel measurement, deterministic channel simulation, and modelling itself.

2.1.4.1 General propagation characteristics

When considering propagation in the mm-wave band, one of the aspects to consider in the design of such radio links is the attenuation due to gases in

the lower atmosphere and rain. Figure 2.16 displays the specific attenuation in dB/km due to oxygen absorption and water vapour for frequencies between 1 to ∼300 GHz. In the frequency range up to 100 GHz, two peaks are visible, one due to oxygen at 60 GHz and the second peak at about 22 GHz due to water vapour. Though the high loss of up to 15 dB/km at 60 GHz prevents from transmission distances in excess of around 1 km, it can be used to advantage for frequency reuse and for secure communication. Losses due to rain can be on the order of 10 dB/km at 25 mm/h increasing to 30 dB/km at 100 mm/h rainfall. They can be crucial at longer transmission distances. However, if only short links below, e.g., 200–300 m are targeted, the losses are less significant. Another factor to consider is the penetration loss due to building material. Whereas coverage in buildings can usually be achieved easily in the classical mobile bands, solid walls become increasingly impenetrable at mm-wave frequencies. These additional losses will either require compensation through higher effective radiated powers or indoor coverage needs to be accomplished by other means.

In principle, a greater amount of rough-surface scattering is to be expected due to the smaller wavelength compared to the STD of surface-roughness, especially for walls made of rough concrete, bricks and other construction materials. Although a stronger DMC at mm-wave frequencies have been hypothesised compared to ultra high frequency (UHF), recent studies have shown that the actual ratio of the DMC to the specular component is similar to what have been observed at UHF [DFM+14] or even lower [HJK+14].

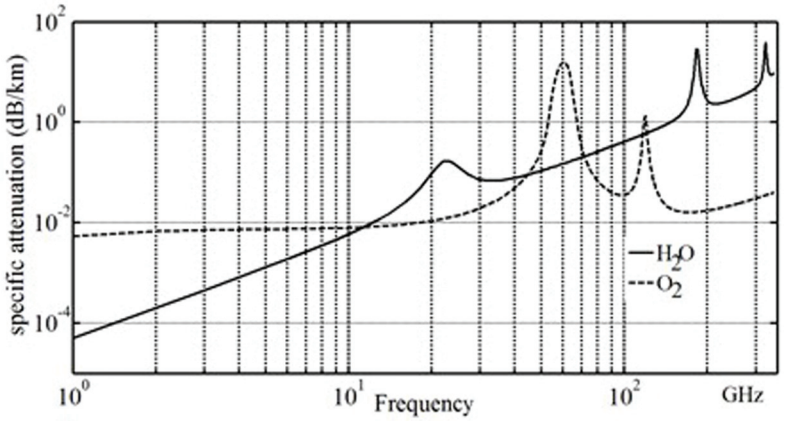

Figure 2.16 Specific attenuation versus frequency due to atmospheric gases: oxygen and water vapour.

This could be due to the lower level of multipath-richness. This aspect is very important to properly design and assess the performance of beamforming techniques recently proposed to enhance the SINR and to implement spatial multiplexing in future multi-gigabit transmission systems.

2.1.4.2 Channel measurement campaigns and results

Due to the large propagation loss and the low-power budget at mm-wave bands, the fundamental concern is the feasibility of NLoS links or of LoS links exceeding 200–300 m range. Therefore reliable PL and shadowing models are of vital importance for the design of mm-wave radio links. In addition, detailed information on the spatiotemporal characteristics of the channel are required for the development of appropriate channel models.

Two types of PL models have been proposed: Hata-like PL models based on measurements [PAC12, RSM$^+$13, HCKP14, RJSJ14, SRC14a, KWPW14] and a dual-slope PL model for 28 GHz outdoor links based on RT simulations in downtown Ottawa, Canada [HCB$^+$14].

In the work by Rappaport et al. [RJSJ14], wideband 28 and 73.5 GHz propagation measurements were performed at 75 distinct RX locations for three separate TX locations in Manhattan, for distances ranging from 30 to 200 m. For large distances, horn antennas with 24.5 dBi (10.9° beamwidth) at 28 GHz and 27 dBi (7° beamwidth) at 73.5 GHz were used at both the TX and at the RX. In NYU campus, the PL exponent in the NLoS condition was estimated as 3.4 at both 28 and 73.5 GHz.

Channel measurements at 28 GHz were conducted using the synchronised rotating channel sounder in different environments which included in building, outdoor campus, and urban environments for distances from 14 to 200 m [HCKP14]. Directional horn antennas with 24.5 dBi gain were used at both the TX and RX. The measurement angle in azimuth was set to cover all directions by rotating the transmit and receive antennas, from 0–360° while the elevation angle range of the RX was selected within –60–60° according to the measurement environment. The omni-directional PL model was then derived after synthesising the omni-directional channel. Figure 2.17 shows the aerial view of the urban environment. The PL exponent was then estimated assuming a reference of 1 m free space loss. The PL exponents and shadowing factors are summarised in Table 2.11.

A new multiband frequency-modulated continuous wave (FMCW) channel sounder with 4.4 GHz bandwidth and 2×2 MIMO capability which uses intermediate frequency (IF) at the TX and fully parallel reception with high dynamic range after back-to-back as well as over-the-air calibration was used to perform measurements in a reflective office environment at 60 GHz

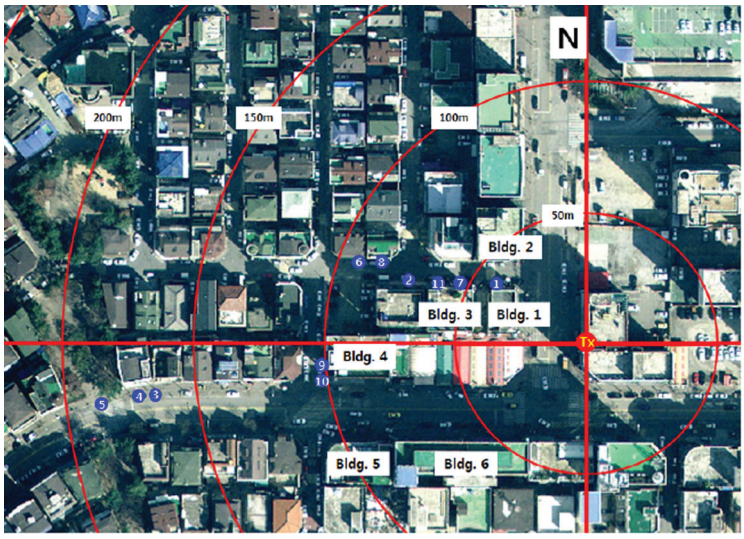

Figure 2.17 PL measurement urban area at 28 GHz.

Table 2.11 The PL parameters

	d (m)	PLE, n	SF, σ (dB)
In-building LoS	$10 < d < 60$	1.91	3.29
In-building NLoS	$10 < d < 60$	3.08	8.92
Campus NLoS	$100 < d < 300$	2.68	7.54
Downtown NLoS	$40 < d < 300$	3.00	6.30

with a wireless local area network (WLAN)-oriented antenna arrangement for distances between 9.4–35 m [SRC14b]. The measurements yielded a PL exponent of 1.87. The median RMS delay spread revealed to be highly dependent on the applied relative threshold and values of 0.42, 5.13, and 8.46 ns were derived for 20, 30, and 40 dB threshold levels, respectively. This shows that only the most dominant components are captured if a 20-dB threshold is applied.

The same channel sounder was used to carry out 2×2 MIMO outdoor measurements at 60 GHz in a representative small cell LoS scenario at the science site of Durham University [SRC14a] covering ranges up to 200 m, with directional antennas with a nominal 20.7 dBi gain and 15.4° azimuthal angular width. A PL exponent of 1.93 was derived. The delay spreads calculated over all four MIMO channels are given in Table 2.12

Outdoor measurements at 70 GHz in the courtyard at the campus of TU Ilmenau for distances up to 45 m have been performed using a novel

Table 2.12 RMS delay spread for small cell measurements at Durham University (60 GHz) and TU Ilmenau (70 GHz) with different threshold (Th) levels

	60 GHz [SRC14a]		70 GHz [MDS$^+$14]	
	20 dB Th		30 dB Th	
	LoS (ns)	NLoS (ns)	LoS (ns)	NLoS (ns)
95% CDF value	2.34	106.9	94.30	
50% CDF value	1.17s	34.64	65.34	

UWB dual-polarised ultra-wideband multi-channel sounder (DP-UMCS) [MDS$^+$14] based on a 12 stage M-sequence radar chipset [SHK13]. Using dual polarimetric antennas, the vertical and horizontal characteristics are measured in parallel at the RX with fast switching between horizontal and vertical polarisation at the TX.

The measurements were performed with circular dual-polarised horn antennas with a 3-dB aperture angle of 14° and a maximum gain of 21 dBi. In the work by Müller et al. [MDS$^+$14], results for vertical polarisation are presented for delay spread. For LoS and with (30 dB threshold) the delay spread varied between 18 and 107 ns. The lowest delay spread was observed for the highest receive powers mainly in the direction of the maximum antenna gain. The delay spread for the NLoS measurement shows values from around 36–94 ns. The 95% CDF values and the 50% CDF values are also given in Table 2.12. In the power Azimuth spectrum (PAS) first and second order reflections were observed. The average attenuation per reflection in the investigated scenario was around 20 dB. The results indicate that transmission ranges of several hundreds of metres are feasible at 70 GHz and even NLoS conditions might be supported by exploiting strong reflections from surrounding buildings, where double reflections can also contribute energy to the link budget.

Several 60 GHz, outdoor measurement campaigns were carried out in the framework of the MiWEBA project [MiW14]. Omni-directional as well as directional antennas were used in combination with two different wideband channel sounders providing 250 and 800 MHz bandwidth, respectively. The omni-directional setup allowed to capture the time-variant characteristics of the busy urban environment, including human body shadowing, as well as the effects of a mobile RX. Several million channel impulse responses were captured to provide a reliable data base for statistical analysis. The directional measurements focused on the investigation of the ground reflection. Overall, the measurements confirm that the ground reflection contributes to the channel in small cell scenarios and that the channel can by highly time-variant, even

for a stationary user. On the basis of these findings and the acquired data a quasi-deterministic (Q-D) modelling approach was derived [MPK+14]. The estimated PL exponent for the LoS-dominant street canyon scenario was 2.13 [KWPW14].

The data from the 28-GHz measurement campaign in the work by Hur et al. [HCL+14] were analysed to extract the cluster parameters such as the number of clusters, N, the number of sub-paths, M and angular information. These parameters can be used for modelling the channel and the extracted parameters are summarised in Table 2.13.

2.1.4.3 RT investigations

Considering the propagation characteristics at mm-wave frequencies, deterministic ray models such as RT or ray launching seem to represent the natural base to model mm-wave propagation [SDNH14]. Being founded on a sound, albeit approximate, theory such as ray optics, ray-based models can be considered fairly reliable when the wavelength is small compared to the size of the obstacles and when the propagation environment is limited and, therefore, a detailed environment description is possible. Recent investigations show that diffuse scattering can be observed in the mm-wave band, but specular propagation mechanisms clearly dominate over DMC. In the work by Haneda et al. [HJK+14] 75–90% of the total power could be attributed to specular components, whereby the dominance was found to be more pronounced in larger environments. The limited degree of DMC could be due to the presence of smooth surfaces in the considered indoor environments. However, outdoor measurements indicate that also the urban mm-wave channel is mainly constituted by several strong components related to specular reflections [MPK+14, MiW14, RSM+13]. With respect to UHF frequencies, comparably small objects such as lamp posts, trash cans and metal window frames seem to have a significant, but more specular-like effect. Depending on the targeted accuracy, it can therefore be important to include them in the model. This especially applies to environments without smooth, planar surfaces and NLoS scenarios [MAB15]. However, in many cases, a deterministic model might not be reasonable anymore due to the unpredictable shape and position of the objects, so related reflections are to be treated as scattering and modelled in a statistical manner [DFM+14, MAB15].

Overall, RT approaches have to be further evaluated for centimetric and millimetric wavelengths. This also includes appropriate modelling of vegetation. In the work by Oesteges [Oes14], a RT tool accounting for vegetation effects is compared with continuous wave (CW) measurements at 12 and 30 GHz in a street canyon carried out in late summer and winter to

Table 2.13 Cluster-based channel model parameters in indoor building-scale environment and outdoor campus environment

Environment	In-Building				Outdoor Campus			
	LoS		NLoS		LoS		NLoS	
Parameters	Mean	Std	Mean	STD	Mean	STD	Mean	STD
Mean Excess Delay (ns)	6.81 ns	10.95 ns	20.17 ns	19.40 ns	45.95 ns	33.34 ns	48.09 ns	65.74 ns
RMS Delay Spread (ns)	5.94 ns	13.10 ns	18.73 ns	19.43 ns	28.68 ns	26.04 ns	34.98 ns	47.25 ns
Number of Clusters, N	1.26	0.63	2.24	1.01	1.77	0.52	1.81	0.80
Number of Sub-paths in Cluster, M	5.17	2.72	10.91	10.48	6.76	4.37	8.59	17.18
Angle Spread - Departure (ASD) (°)	8.80	11.61	10.45	10.27	4.39	0.47	6.60	3.36
Angle Spread - Arrival (ASA) (°)	5.84	5.32	21.88	17.49	4.39	0.94	9.54°	12.55
Intra-cluster ASD (°)	7.71	10.60	11.52	12.70	4.34	0.73	5.54°	2.59
Intra-cluster ASA (°)	4.72	2.69	11.84	13.35	4.19	1.28	5.87°	7.62

investigate the impact of two deciduous trees obstructing the line of sight. Corrugated circular horns with vertical polarisation were used with 20° beamwidth at the TX and 30° at the RX. Measurements were taken when the antennas were aligned on a 60-m TX track in the street with 1 m spacing, and the RX was fixed on a building.

Using the well-known Fresnel theory and the uniform theory of diffraction (UTD), the RT tool accounted for single-reflected rays by walls and the ground, single diffraction by building wedges and attenuation by trees. Diffuse scattering and transmission through buildings were neglected. Regarding vegetation, only the tree foliage was modelled by means of parallelepiped blocks applying the ITU-R 236-6 recommendation to calculate the attenuation [CCI86]. Despite the simple simulation model, good agreement between the simulations and the measurements of the average received power could be achieved for both frequencies.

According to Oesteges [Oes14] slightly rough surfaces at small wavelengths can be accounted for by introducing a reduction factor with respect to free-space propagation and Fresnel reflection for the specular reflections. Given the roughness of typical walls, e.g., brick walls, the diffuse component contribution at mm-wave frequencies is often negligible compared to the specular one. The diffuse power can be assessed by applying the Kirchhoff approximation or the first order pertubation solution, which better accounts for polarisation effects [Oes14, COS01]. However, diffuse scattering can become important if very directive antennas are used in NLoS scenarios.

Parameters estimated from measurements are limited by the resolution of the radio measurement equipment. RT on the other hand models only specular reflection, edge diffraction, and penetration. However, according to Takada et al. [MGI06], scattering cannot be ignored comparing the measurements with the RT simulation results in visualised photos which can be helpful to understand the propagation mechanisms. In Tsuji et al. [TKT14], visualisation of the propagation channel is compared with the radiophotos of the measurement and the simulation results. In Figure 2.18, the direct wave is appropriately reproduced in the simulation. However, the possibility remains that some reflections are underestimated in the simulation and scattering might not be considered.

2.1.4.4 Stochastic and semi-stochastic mm-wave channel models

Since the application of mm-wave transmission to mobile communication is closely linked to the exploitation of beam forming and MIMO techniques, multidimensional propagation models accounting for time and angle

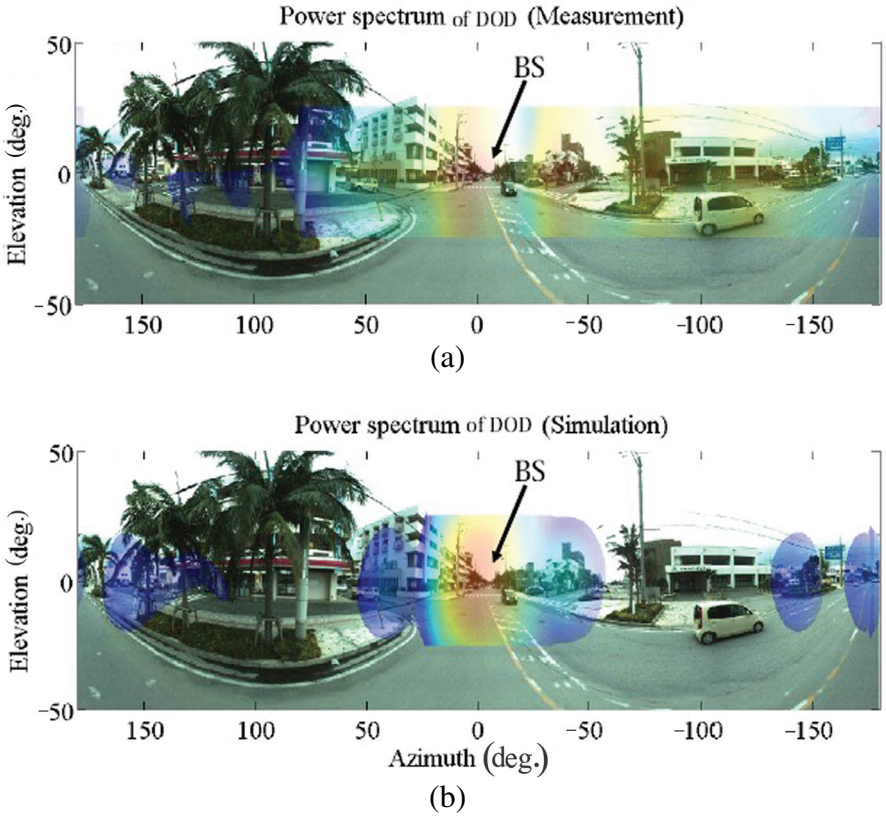

Figure 2.18 DOD radiophoto: (a) measurement and (b) simulation.

dispersion of the signal are required. Several models for 60 GHz indoor applications have been developed within standardisation bodies such as the statistical channel model IEEE 802.15 TG3c [Yon07] and the IEEE 802.11ad geometric-stochastic channel model [MMS+10]. The latter is based on a mix of deterministic RT and measurement-based statistical modelling techniques and on the concept of multipath cluster [HJK+14].

However, for cellular mm-wave transmission there is no channel model for outdoor long-distance range. Due to the long-distance range and the directional measurements, only limited measurement campaigns were conducted to extract angular spread. An extension of the standard channel model used in the ITU and 3GPP, to the mm-wave channel modelling in cellular system is proposed in the work by Hur et al. [HCKP14]. From the measurements, the spatio-temporal channel characteristics such as multipath delay, angular

statistics, and PL are analyzed including clustering analysis. The corresponding channel models based on the 3GPP spatial channel model (SCM) are proposed with a set of mm-wave radio propagation parameters. Procedures similar to 3GPP SCM [3GPP10] and WINNER II model are applied to extend the model to cover mm-wave systems up to 250 MHz bandwidth with the proposed subpath delay/AoD/AoA distributions in the work by Hur et al. [HCKP14].

There is also a trend towards the introduction of deterministic elements into geometry stochastic channel model (GSCMs) to derive "map-based GSCM" models [MBH+14]. In the framework of the FP7 MiWEBA project a novel Q-D approach for modelling outdoor and indoor mm-wave channels is proposed [MPK+14, MiW14]. The Q-D modelling methodology is based on the representation of the channel impulse response as the superposition of a few Q-D strong rays (D-rays) and a number of relatively weak random rays (R-rays) and flashing rays (F-rays). D-rays can, e.g., be related to the direct and the ground-reflected ray. In the model they are explicitly calculated from geometry. R-rays and F-rays are attributed to faraway or moving ("flashing") reflectors and defined by random variables. Following this methodology, models for open area (university campus), street canyon and hotel lobby scenarios have been developed. They have been verified and parametrised by two independent 60 GHz channel measurement campaigns carried out by Intel and Fraunhofer HHI. The explicit introduction of deterministic and random rays enables the modelling of real dynamic outdoor environments, taking into account mobility and blockage effects. Moreover, the versatility of the Q-D methodology allows extending the developed model to other usage cases with the same environment geometries like device-to-device (D2D) and street-level backhaul links.

2.2 Urban Reference Scenarios

For the development and the evaluation of mechanisms for mobile networks, an adequate system model is an important foundation. To define a system model, different modelling and design decisions have to be considered depending on the evaluated effects. However, deviating assumptions and implementations of such models render it difficult to compare and reproduce research results. Common simulation scenarios are therefore important for the efficiency and quality of research, Section 2.2.1 gives an overview over different modelling approaches and summarises efforts to align the results of independent simulators.

Widespread simulation scenarios, like those proposed by the 3GPP, rely on regular geometries and uniform user distributions. Thus, they cannot represent the fine shades of real or realistic, complex, heterogeneous environments. In order to provide actual means for the research community to shift from simple simulation assumptions to a far more reasonable degree of detail – at lowest costs and efforts – the *Hannover Scenario* is designed to provide a common simulation environment in the city of Hannover, Germany, as described in Section 2.2.2. It ensures the comparability of simulation results, which are based on this scenario. Furthermore, it allows researchers bringing their focus back to the actual development of smart algorithms instead of reinventing simulation scenarios again and again. For this purpose, a complete LTE network has been modelled for the entire city area of Hannover.

2.2.1 Simulators for Urban Environments

For the evaluation of urban environments, typically system level simulators are used to grasp the complexity of interactions between multiple cells. Simulations can either be dynamic, i.e., chronologically modelling the reaction of the system to events, or static, i.e., analyzing a fixed environment.

Static simulations are often used for site planning or other long-running optimisations. In del Apio et al. [dAMC+11], the authors compare the energy efficiency of different cell deployments in the same static scenario. They show that adding femto cells to a traditional network layout leads to a significant improvement of system performance and energy efficiency. To plan the placement of femto cells, Deruyck et al. [DTJM12] presents a network planning tool which is based on abstract and efficient channel models and heuristics. As more cells are added to a system, interference becomes an even more relevant topic. To preserve sufficient system performance also for cell border users, the optimisation of power and bandwidth allocation is performed by Krasniqi [KMM11] based on simplified static scenarios.

Dynamic simulations serve to incorporate dynamic effects of user behaviour, e.g., mobility and traffic patterns. They have to be applied whenever algorithms or control loops operate iteratively over a range of time. The temporal granularity of the simulations has to be chosen to match the evaluated algorithms and effects. The comparison of self-organising network (SON) algorithms to tune handover parameters and transmit power for load balancing is simulated with a 100-ms interval in the work by Ruiz-Avilés et al. [RALRT+11, RLTR12, HRK14]. In contrast, to evaluate the quickly reacting uplink power control algorithms of LTE, the temporal granularity

of the simulation has to be increased to 1 ms [LGOR11, LGRO+11]. The same fine temporal granularity is required for the investigation of scheduling algorithms as presented in the work by Robalo et al. [RVPP15].

For static as well as dynamic simulations, one can apply either synthetic or realistic scenarios. Typical example for a synthetic scenario are the simulation guidelines published by 3GPP [3GPP10]. BSs are placed in a regular hexagonal grid and user mobility is modelled randomly. In contrast, realistic models strive to use scenarios from the real world as prototypes.

In Uppoor et al. [UF12, UTFB14], the authors have built a realistic model for urban road traffic in the city of Cologne, Germany. The model is based on freely available street data and on the TAPAS Cologne project, which derives traffic demands from a large survey. To get realistic traffic density, some manual corrections to the data were required. The authors show that, by using this model in simulations, relations between cars are significantly different from those evaluated with coarser mobility models. The risk of overly simplified models is also pointed out by the publication [HRK14]. There, the authors show that the performance of SON algorithms for load balancing significantly differs between synthetic and realistic scenarios.

The trend to use realistic models is also seen in Hahn et al. [HRK14], Deruyck et al. [DTJM12], del Apio [dAMC+11], and Lema et al. [LGRO+11]. However, evaluations based on realistic models often lack comparability. One of the reasons is that data sources are often not freely accessible, as they are, e.g., based on confidential information of network operators or collected commercially and their usage is subject to a fee. To ease the sharing of geographical data, a data format for exchange is proposed in the work by Navarro and Londoño [NL14]. Also, in Subsection 2.2.2 a publicly available scenario is presented, which can be used for cellular network simulations.

Institutions do typically use different simulation programs for their evaluations. These are often self-implemented [RALRT+11, LGOR11, CIJW13], but there are also commercial [XS12] and open source simulators [MCIŠ+11, RVPP15] available. For the scientific community, it would be good to have comparable and reproducible simulation results. However, it is often difficult to reproduce simulations from the model specification given in a publication.

In Colom Ikuno et al. [CIJW13], the authors describe their effort to align simulation results of three simulators. The compared implementations are the LTE System Level Simulator implemented at the Vienna University of Technology [MCIŠ+11], the SiMoNe Simulator implemented at the Technische Universität Braunschweig [RBHK15], and the IKR RadioLib implemented at the Universität Stuttgart [IKR15] (based on the work by Sommer and Scharf

[SS10]). The focus of the Vienna simulator lies on good mapping of link level results and realistic TP prediction. In contrast, the SiMoNe simulator implements realistic cell layouts and user mobility, which is required to evaluate SON algorithms. The IKR RadioLib is typically used with synthetic scenarios to evaluate cross-layer effects and interactions of cells in Cloud-RAN systems. The latter two simulators employ rather abstract models of the physical layer to achieve higher simulation performance. This is required to evaluate SON algorithms and effects from data traffic, which operate on longer time frames and thereby require longer simulated times.

Two scenarios have been chosen for comparison. In the first scenario, a single cell with isotropic antenna is used to align the calculation of PL and the mapping of SNR to spectral efficiency. The evaluations show that the results match well. The second scenario consists of multiple interfering hexagonal cells and follows the definitions in [3GPP10]. Evaluations in this scenario show a good match for the RSRP of the mobiles, but only if shadowing is disabled. Although the compared simulators implement similar shadowing models, the different configuration of correlations between adjacent sectors and the interaction between shadowing and placement of users into cells results in different RSRP distributions. More deviations occur at the evaluation of spectral efficiency. These are probably caused by differences in the abstraction of the physical layer, i.e., the mapping of wide-band SNR to TP. In addition, the scheduling algorithm and granularity also influences these results. It proved to be difficult to achieve an exact match of simulation results, because the used simulators were designed for different applications. It remains an open task for the research community to improve comparability and reproducibility of simulation results.

Simulation guidelines and scenarios (like published by 3GPP) and widely accepted models (like the Winner II channel model) are a good starting point to facilitate comparability, but they do still leave aspects and implementation details open. In addition, studies of effects on different layers and time scales require problem-specific abstractions. If in the common guidelines relevant effects are not modelled with the required accuracy, it is inevitable to deviate from these guidelines. In addition, many small design and parameter decisions, which are not covered by published scenario descriptions, can have influence on the results. One way to ensure a comprehensive specification of the simulation model and to ease reproducibility is to publish the whole source code used for the simulations [MCIŠ+11]. However, retracing foreign source code can be a time-consuming and error-prone task. As an

alternative, the usage of predefined scenario data might help to mitigate this problem. The following subsection describes a common scenario based on publicly available trace files. By using these trace files in simulations, less effects have to be modelled in the simulator, which eases comparison and reproduction.

2.2.2 Hannover Scenario

As stated above, the *Hannover Scenario* is designed to provide a common simulation environment in the city of Hannover, Germany. For this purpose, a complete LTE network has been modelled for the entire city area of Hannover. By using real 3D building data, it allows for realistic PL predictions and realistic network planning. In addition, sophisticated modelling approaches for macroscopic traffic and individual user mobility have been employed, in order to get a realistic baseline for the simulation of subscribers in the network. The described scenario provides the starting point for the development and implementation of the mentioned SON algorithms. They might also be used in context with other advanced network algorithms, which take the timely varying channel conditions of a plethora of different users into account.

Nevertheless, the current simulation scenario is subject to change. Most probably, this process will reveal simulation and/or environmental aspects that need to be optimised in future versions of the simulation scenarios, in order to cope with the special requirements of the individual cases. In order to ease the initial work, the scenario definitions of the *Hannover Scenario* are provided as traces in a common input format, which is explained in detail in the work by Rose et al. [RJT+13].

2.2.2.1 LTE network in the Hannover scenario

The current evolution of this scenario consists of a macro cellular network, which covers mainly the suburban and urban regions of the city of Hannover. The area of the *Hannover Scenario,* for which the network is planned, spreads over 20×24 km^2. In order to minimise border effects in actual simulations, an area of only 3×5 km^2 is considered for simulation purposes and will be used for the collection of user and/or cell statistics. All mobile and static users reside in the inner area, only. Besides, all PL predictions for this scenario are currently made for a height of 1.5 m above ground. In the future development of this scenario, PL prediction layers for different heights are planned. In particular, to cope with the effects of moving users in buildings

Table 2.14 States the relevant aspects of this scenario and the provided models

Scenario	LTE 1800
Coordinates of the planned area (m)	E: 00000 ... 20000 (20 km) N: 00000 ... 24000 (24 km) E_{gk4}: 4336000 ... 4356000 (20 km) N_{gk4}: 5794000 ... 5818000 (24 km) 480 km^2
Coordinates of the scenario area (m)	E: 08500 ... 11500 (3 km) N: 11000 ... 16000 (5 km) E_{gk4}: 4344500 ... 4347500 (3 km) N_{gk4}: 5805000 ... 5810000 (5 km) 15 km^2
Macro cells	LTE 1800: 195 TX power: 46 dBm
Smaller cells	None
Mobility patterns	Static users (10000) Vehicular users (4620) Pedestrian users (5247)

[RJHK13] and indoor deployments of pico and femto cells on different storeys [RJK11].

The BSs used in this scenario are realistic, which means *close to the reality,* but nevertheless artificial. As for the modelled area no information of real BS configurations is publicly available, the model is based on data from the regulatory authority and on publicly reported sites. Based on this data, a single-layer network for LTE 1800 has been planned, using an iterative process of optimisation. Briefly explained this means, after each step of network geometry planning, the network's coverage has been predicted and analysed for coverage holes. Finally, this process resulted in the network presented herein: In total, 195 sectors for the 1800 MHz band have been planned.

Figure 2.19 shows the geometry of the macro cellular network at 1800 MHz for the whole planned area of 20×24 km^2.

2.2.2.2 User mobility models

One very important aspect in system-level simulations is the change of the environment over time especially in terms of varying spatial traffic. This means, for the simulations of individual user movements, the users' positions are generated using different approaches, ranging from static indoor users to highly mobile users, as briefly described in the following subsections.

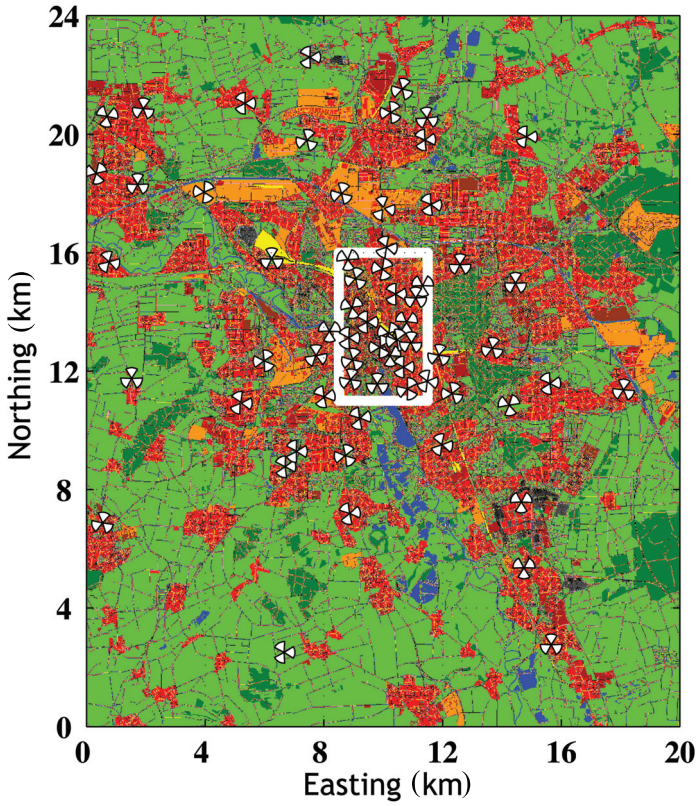

Figure 2.19 Network geometry for LTE 1800.

Static users

The simplest form of user *mobility* is actually where the position remains constant over time. These static users are useful in order to generate network traffic, which is associated with certain positions but no actual movements. All static users are located indoors.

Vehicular users

Vehicular users are generated using a highly realistic simulator, named SUMO (Simulation of Urban MObility). SUMO is a freely available microscopic road traffic simulator [DLR14], which simulates cars travelling along the streets. The actual mobile users are inside their cars. The simulation capabilities of SUMO include lane changes, overtaking of cars and acceleration and

deceleration. Especially in situations close to junctions or crossings a queue in front of the traffic lights can be observed or the following of right-of-way rules. In other words, the simulated users are interacting with each other, which lead to very realistic user positions and movements.

Pedestrian users

Pedestrian users are generated by using a simulation approach stated in the study by Hahn et al. [HRSK15]. The resulting traces are representing individual users, which follow an aim-oriented behaviour. Besides paths that are provided as sidewalks in the geographical database, automatically generated short cuts a pedestrian might also take when leaving the path are considered. The contained traces simulate users on their way moving from an entry point of a building to another one, the route in between is determined by a routing algorithm.

2.2.2.3 Propagation models

In this subsection the principle process to derive PL predictions is described. The propagation models are sketched along with their general settings and considerations, which had been used for the creation of the *Hannover Scenario*. Since three-dimensional building information has been accessible for the city of Hannover, a ray optical model is best suitable for PL predictions in this area. More details on ray optical modelling, in particular on RT and ray-launching can be found in the work by Lostanlen and Kürner [LK12].

Ray optical outdoor predictions

A RT model (called the ray tracer), has been used to predict the outdoor coverage of the cells in this scenario. This predictor looks for the ray optical propagation paths between the TX and the RX antennas. The ray tracer follows the concept of sub-dividing the model into sub-models as described in Kürner [Kür99] and Kürner and Meier [KM02]. Here, a vertical plane model (VPM) and a multi-path model (MPM) have been used. The MPM model is based on the approach described by Kürner and Schack [KS10] and recognises the following types of paths:

- Reflected paths are considered up to the second reflection. Reflections can have a maximum image source distance [LK12] of up to 1000 m [Kür99].
- Scattered paths are considered up to a maximum distance of 500 m between the TX and the RX. Scatterers are searched up to a distance

of 550 m around the BS according to the findings in the work by Kürner [Kür99].

The VPM uses the following approach:

- In case of LoS the PL is calculated based on a distance dependent selection, which uses the free-space propagation loss (up to 200 m), the Okumura–Hata model with sub-urban correction (beyond 500 m) and a transition model in between.
- In case of NLoS the paths over the roof-tops are considered. The total PL is the sum of the PL (as stated for the LoS case) and a diffraction loss calculated according to Deygout [Dey66].

Outdoor-to-indoor predictions

The prediction of areas covered by buildings is done in a subsequent step, based on a *Ground Outdoor-to-Indoor* approach [GB94, RK12]. *Ground Outdoor* refers to the outdoor coverage at ground level, which is usually predicted for mobile terminal heights of 1.5 m. The signal level on the inside at ground level is directly related to the coverage on the outside at the same height. The prediction model is described in the work by Rose and Küner [RK12]. According to this publication, outer walls are contributing with very individual attenuations between 5 and 20 dB. So a general attenuation of 10 dB has been chosen for the predictions, which has also been used in other publications [OKI09, HWL99]. Based on the distance between the respective indoor position and the outer wall, a linear attenuation of 0.8 dB/m is added to the PL, according to the findings reported in the work by Rose and Küner [RK12].

2.2.2.4 Data traffic model

Besides the user mobility, the load of the cells in a cellular system is mainly influenced by the data traffic the users generate or request from the Internet. Simple models like full buffer or fixed rate do often fail to capture the dynamics of real Internet traffic. Therefore, we provide a model which is based on measurements in mobile and fixed networks. The dynamics of Internet traffic are mainly influenced by two effects: on a large time scale, the user or an autonomously acting application decides to send or request a certain amount of data. On a smaller time scale the transport protocol (typically TCP) fragments this data into packets and controls the rate at which these packets are sent. While the start times and the size of requests and responses can be pre-calculated and stored in trace files, the behaviour of TCP directly depends

on the actions of the mobile network, especially the scheduling. Therefore, the behaviour of TCP has to be either modelled in the simulator or these effects have to be approximated.

2.2.2.5 Conclusion and future work

The presented IC 1004 Urban Hannover Scenario delivers a variety of scenario data in a realistic simulation environment. The currently available data set is a first step towards more complex and modular simulation scenarios and system simulations. It is hoped that the utilisation of a freely available, ready-to-use and easy to implement simulation scenario will ease the comparison of simulation results in the future. Feedback from the scientific community on the usability and completeness of the present scenario data will help to improve the data set for new research activities.

2.3 Summary and Future Directions

Prediction of the performance of radio networks in the diverse urban environment requires a variety of techniques. Deterministic models dictate the use of scenarios with known propagation characteristics, while empirical models are limited by the number of measured scenarios. To this end we propose the use of the Hannover scenario for common simulations. Results of studies in a variety of urban scenarios below the 6 GHz band including the challenging environments of trains and containers and the emerging massive MIMO technologies have been presented in this chapter as well as vehicular scenarios. Preliminary results of propagation measurements in the mm-wave band in line of sight scenarios indicate PL exponents close to free-space propagation on the order of 2 with the use of directional horn antennas. Higher coefficients of 3 have been estimated for non-line of sight scenarios. Delay spread values of LoS and NLoS in environments in the 60 and 70 GHz bands for two outdoor scenarios with single and dual antenna configurations give values varying from 2.3 to 94.3 ns for 95% of the measured locations. However, the number of measured scenarios is currently very limited to a few sets of data to draw comprehensive conclusions and the results are system dependent that further extensive measurement campaigns are needed to extract and validate the relevant channel parameters. A major challenge in the mm-wave band studies is to de-embed the antenna pattern from the measured channel since currently due to limited transmit powers, propagation studies are performed using high gain directional antennas. The deployment of an antenna array that enables such studies is a major challenge where fast switching to cover

the high Doppler shifts in urban mobile environments would be needed. Due to the complexity of such measurements, RT approaches or a combination of RT and stochastic models are being proposed. Detailed information regarding the environment and the electrical properties of the materials are needed in RT modelling which can be a challenge. Further research to investigate the feasibility of beamforming, tracking, and interference between links in the mm-wave band is still at an early stage and requires further investigation.